DETERMINATION OF OPTICAL, ELECTRICAL, STRUCTURAL, AND MORPHOLOGICAL PROPERTIES OF $MAPbI_3$ PEROVSKITE FILMS FOR PHOTOVOLTAIC APPLICATIONS

ABOK SILAS ODHIAMBO

A Thesis submitted in Partial Fulfillment of the Requirements for the Conferment of Degree of Master of Science in Physics of Masinde Muliro University of Science and Technology

November 2025

DECLARATION AND APPROVAL

Declaration

This thesis is my original work, prepared with none other than the indicated sources and has not wholly or in part, been submitted for the award of a degree in any other university or higher learning institution.

Signature……...Date…….

Abok Silas Odhiambo

SPH/G/01-70556/2021

Approval

The undersigned certify that they have read and hereby recommend for acceptance of Masinde Muliro University of Science and Technology a research thesis entitled "**Determination of the Optical, Electrical, Structural, and Morphological Properties of $MAPbI_3$ Perovskite Films for Photovoltaic Applications**".

Dr. Celline Awino Omondi

Masinde Muliro University of Science and Technology, Department of Physics.

Signature:  Date: 2nd June 2025

Dr Francis Magiri Gaitho

Masinde Muliro University of Science and Technology, Department of Physics

Signature…….……Date…….

PLAGIARISM STATEMENT

Student's Declaration

I hereby declare that I discern that the incorporation of materials from other research works or a paraphrase of such materials without acknowledgment will be subject to plagiarism, the thesis must be my own original work as per the Rules and Regulations of Masinde Muliro University of Science and Technology.

I know that plagiarism is academic dishonesty and wrong and that if I commit any act of plagiarism, my thesis can be assigned a fail grade ("F"). I further understand that I may be suspended or expelled from the University for Academic Dishonesty.

Name……Signature…..……

Registration Number ……. Date…….

Supervisors' Declaration

We hereby approve this thesis to be subjected to examination and declare that the content has been subjected to a plagiarism test and its similarity index is not more than 20%.

1) Name: Dr. Celline Awino Omondi Signature  Date: ……..

2) Name : Dr. Francis Magiri Gaitho Signature……Date…….

COPYRIGHT

This thesis is copyright materials protected under the Berne Convention, the copyright Act 2001 and other international and national enactments on that behalf, on intellectual property. It may not be reproduced by any means in full or in part except for short extracts in fair dealing so for research or private study, critical scholarly review or discourse with acknowledgement, with written permission of the Directorate of Postgraduate Studies on behalf of both the author and Masinde Muliro University of Science and Technology.

©2025 Abok Silas Odhiambo

DEDICATION

This entire work is dedicated to my humble and kind-hearted mum, Terry, for her unceasing prayers and my caring brother, Eng. Thomas Abok for always providing me with the necessary support and motivation through sacrifice despite other family responsibilities.

ACKNOWLEDGEMENT

I earnestly thank those who helped me, by advice, example or otherwise, in bringing this work to completion. At the top of my list I would like to thank Almighty God who has given me this life and the persistence in completing this study.

My gratitude is beyond measure to my supervisors, Dr. Celline Omondi and Dr. Francis Gaitho of Masinde Muliro University of Science and Technology whose professional opinions, boost and consistent motivation saw me through-particularly in times of uncertainty.

Lastly, I would like to take this opportunity to thank my colleagues in the Department of Physics, and all of the members of the Department of Physics, as a whole, for their encouragement and support in creating an atmosphere in which I could pursue this research to fruition.

ABSTRACT

The study presents a combined analysis of optical, electrical, structural, and morphological properties of methylammonium lead iodide ($MAPbI_3$) thin films as solar cells. Four MAPbI 3 samples were prepared and characterized via UV Vis spectroscopy, X-ray diffraction (XRD), scanning electron microscopy (SEM) and current-voltage (JV) measurements. Based on the optical analysis, it was established that an onset of absorption was sharp around 1.6 eV and that the coefficients of absorption (> 104 cm^{-1}) verified the direct bandgap nature of MAPbI 3. Tauc plot extrapolation gave average optical bandgap values of 1.515 eV and this complies with most appropriate range of single-junction solar cells. The highest value of power conversion efficiency of 13.91 % was observed in the electrical characterization in a forward scan with moderate hysteretic losses that are ion migration and interfacial charge accumulation effects. It was established in the structural analysis that there was a prevalent (110) orientation as well as good crystallinity but larger values of FWHM at the higher Miller indices indicated localized lattice strain and smaller grain domain size. Morphological analysis yielded an average grain size of 196±36nm which were uniform and favorable to efficient charge transport and effective recombination. The large grain circularity and solidity also pointed to the excellent film quality that was attained by optimization of spin-coating thickness with a two-step thermal annealing procedure. These results confirm the suitability of $MAPbI_3$ regarding the usage of thin-film solar cells and elaborate on the significance of processing conditions towards the tailoring of film properties and thus the overall device performance. The study contributes to the body of knowledge regarding the determinants that contribute to enhancing efficiencies, as well as stability in perovskite-based Photovoltaics.

Table of Contents

DECLARATION AND APPROVAL ii

Declaration ii

Approval ii

PLAGIARISM STATEMENT iv

COPYRIGHT vi

DEDICATION vii

ACKNOWLEDGEMENT ix

ABSTRACT x

Table of Contents xi

LIST OF FIGURES xv

LIST OF TABLES xvi

LIST OF SYMBOLS AND ABBREVIATIONS xvii

CHAPTER ONE 1

INTRODUCTION 1

1.1 Background of the Research 1

1.2 Statement of the Problem 4

1.3 Objectives of the Study 5

1.3.1 General Objective 5

1.4 Significance of the Study 6

1.5 Justification of the Study 6

CHAPTER TWO 7

LITERATURE REVIEW 7

2.1 $MAPbI_3$ as a Potential Material for Photovoltaic Applications 7

2.1.2 Properties of $MAPbI_3$ Perovskites 8

2.1.3 The Structure of Perovskites 9

2.2 The Fundamental Operation of Perovskite-based Solar Panels 10

2.4 Solar Photovoltaic Performance Evaluation Parameters 15

2.5 The Solar Spectrum 17

2.6 Charge Transporting Mechanisms in PSCs 20

2.7 Absorption coefficient 22

2.8 Tauc gap 23

2.9 Characterization Techniques for Perovskites 25

2.9.1 X Ray Diffraction (XRD) Technique 25

2.9.2 Scanning Electron Microscopy (SEM) 27

2.9.3 UV-Vis Spectroscopy 29

CHAPTER THREE 31

MATERIALS AND METHODS 31

3.1. Materials 31

3.2 Substrate Preparation 31

3.2.1 Perovskite Film Preparation 31

3.3 Characterization Techniques 34

3.3.1 X-ray Diffraction 34

3.3.2 Scanning Electron Microscopy (SEM) 35

3.3.3 UV-Vis Spectroscopy 35

3.3.5 J-V Scan Photovoltaic Performance Analysis 36

3.4 Data Visualization and Analysis 37

CHAPTER FOUR 39

RESULTS AND DISCUSSIONS 39

4.1 Structural Characteristics of $MAPbI_3$ 39

4.2 Morphological Analysis 42

4.3 Optical Properties 49

4.3.1 The Reflection, Absorption and Transmission Spectra 49

4.3.2 UV-Vis Absorption Edge Analysis 50

4.4 Electrical properties 54

CHAPTER FIVE 63

CONCLUSIONS AND RECOMMENDATIONS 63

5.1 CONCLUSIONS 63

5.2 RECOMMENDATIONS 64

REFERENCES 65

APPENDICES 90

Appendix I: Python source code for IV characteristics 90

Appendix II: Python source code for RAT spectra 91

Appendix III: Python Script for SEM image segmentation 92

Appendix IV: Python source code for Diffraction patterns 97

Appendix V: Glovebox Equipment 99

Appendix VI: The sonicator, spin coater and heater equipment 100

Appendix VII: Film Deposition in the MMUST Perovskite Laboratory 100

LIST OF FIGURES

Figure 2. 1: Ideal ABX_3 structure of a perovskite 9

Figure 2. 2: Adopted Planar inverted Perovskite Architecture 12

Figure 2. 3: Typical I-V and P-V Curve for a solar cell device 15

Figure 2. 4: The Solar Spectrum 18

Figure 2. 5: Schematic of a typical energy level diagram 20

Figure 4. 1: X-ray Diffraction Pattern of $MAPbI_3$(a), lattice spacing for $MAPbI_3$ (b), d-spacing for corresponding miller indices (c) and FWHM vs three dominant miller indices (d) 38

Figure 4. 2: Cross sectional Grain Analysis and Image segmentation at 1000X resolution .. 40

Figure 4. 3: Top view Grain Analysis and SEM image segmentation at 10,000X resolution 42

Figure 4. 4: Cross sectional view Grain size analysis at 10kX SEM image Resolution 43

Figure 4. 5: Cross-sectional Grain size Analysis and Image segmentation at 30,000X resolution 44

Figure 4. 6: RAT spectra (plots of TRA; black, red and blue curves respectively). 45

Figure 4. 7: Absorption coefficient vs Photon energy for the different Samples. 46

Figure 4. 8: Tauc plot for $MAPbI_3$ 49

Figure 4. 9:J-V Characteristic curves for both forward and reverse conditions. 50

Figure 4. 10: PV curves for forward and reverse bias conditions 51

Figure 4. 11: Fill factor and efficiency for the resulting device 52

Figure 4. 12: (a) Variation of FF with Shunt Resistance (Rsh); (b) Variation of FF with Series Resistance (Rs) 54

Figure 4. 13: Average PCE for different samples 56

LIST OF TABLES

Table 4. 1 :Measured electrical parameters from JV Scanning in Reverse and Forward bias 57

LIST OF SYMBOLS AND ABBREVIATIONS

ASTM	American Society for Testing of Materials
BCP	Bathocuproine
$CH_3NH_3^+$	Methyl Ammonium Ion
Cs^+	Cesium cation
EA	Ethyl acetate
Eg	Band gap Energy
ETM	Electron Transport Material
FA	Formamidinium
FF	Fill Factor
FTO	Fluorine doped Tin Oxide
HOMO	Highest Occupied Molecular Orbital
HTM	Hole Transport Material
I	Iodine
Isc	Short Circuit Current
ITO	Indium doped Tin Oxide
*J*sc	Short Circuit Current Density
LUMO	Lowest Unoccupied Molecular Orbital

MA	Methylammonium
$MAPbI_3$	Methylammonium Lead iodide
$NH{=}CHNH2^{+}$	Formamidinium Ion
Pb	Lead
PbI_2	Lead iodide
PCE	Power Conversion Efficiency
Pmax	Maximum Power Point
PSCs	Perovskite Solar Cells
PTAA	Poly[bis(4-phenyl)(2,4,6-trimethylphenyl)amine]
	Spirobifluorene
Spiro-MeOTAD	2,2',7,7'-tetrakis(N,N-di-p-methoxyphenyl amine)-9,9'-
SPVCs	Solar Photovoltaic Cells
STCs	Standard Test Conditions
Voc	Open Circuit Voltage
Φ	Work Function

CHAPTER ONE

INTRODUCTION

1.1 Background of the Research

Photovoltaics is an area that has evolved over the past few years, especially the creation of perovskite solar cells (PSCs) that act as a new horizon to generate solar energy. The perovskite-modeled materials, including perovskite materials, are the potential materials to be used in solar cells because of their high potential in efficiency and the process of fabricating them is a low-cost procedure. Among the different variants of perovskites, Methylammonium Lead Iodide ($MAPbI_3$) perovskites have been found particularly promising as a material in solar cells, with more than 20 percent power conversion efficiency achieved (Kojima *et al*., 2009). Since 2012, the efficiency of perovskite solar cells improved rapidly and, as Figure 1.1 illustrates, by this metric, this period is defined by a rapid increase in efficiency. Now the leader in terms of maximum efficiency of perovskite solar cells is 25.8% (Min *et al*., 2021).

The sun provides a massive source of solar energy amounting to about $3.9x10^{24}$ J on a daily basis (NASA Facts the Balance of Power in the Earth-Sun System, 2005) to the surface of the earth making it a very tough competitor when it comes to satisfying the energy demands of the growing population. Solar photovoltaic cells (SPVCs) are transducers through which solar energy gets converted to electricity. The availability of other extensive materials on earth such as silicon, group III-V compounds, and diverse thin film nanocomposites are very important in the successful and green generation of the

solar cells. Various techniques to fabricating solar cell materials are large wafer basis crystalline silicon, group III-V compound epitaxial layer structures, peripheral thin film structures and even nanotubes.

The largest segment of the photovoltaic market is cryptalline silicon (c-Si) technology that uses p-n junctions to condense more than 90 percent of the solar photovoltaic panels (Kaizuka and Masson, 2017). The availability of Silicon in large quantities in nature attributed to its creditability and as well, the c-si solar cells have moved to be consistent with its long lifespan of more than 25 years which is very impressive (Monier, 2011). Such cells have demonstrated remarkable PCEs of up to 26.7% (Green *et al*., 2018). But there is another problem with the silicon-based wafers i.e. the energy required to create a very pure silicon crystal is very high.

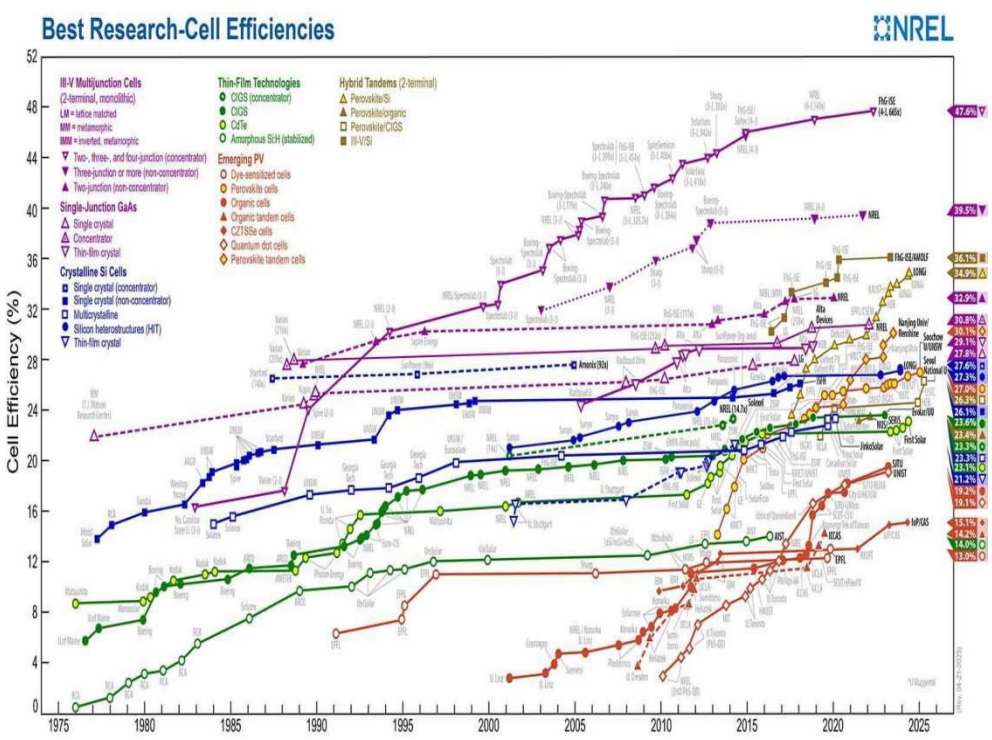

Figure 1. 1*: Progressive Perovskite efficiency increase chart*

(NREL,2023)

The latest reported conversion of power to be done using focused sunlight was efficiently carried out using a semiconductor material comprising of the epitaxial layers of combining group III - v compounds, and was found to have attained an efficiency rate of 46 percent (according to the National renewable Energy Laboratory efficiency chart; 2023) in the multi-junction solar cells. Their efficiencies run as high as 25% yet at the present time group III-V based solar cells based on semiconductors can only be used in space and concentrator applications because they are not of comparable economical price as group I-II-VI produced semiconductor-based cells (Kaizuka and Masson, 2017). On the other hand, thin film technologies are invented in hopes of reducing the cost of manufacturing where the thin film of absorbers is applied on the second substrates like glass. However, the thin film solar cells demands include their lower efficiencies with certain material like amorphous silicon (a-Si:H) and potentially limited availability of materials like tellurium in cadmium telluride and indium in copper gallium indium dis selenide solar cells (Grätzel, 2003).

Nanocomposites are a type of material that is composed of the interpenetrating different phases that are integrated to attain the wanted range of properties. Dye-sensitized solar cells, which represent a prominent sub-group of nanocomposite solar cells developed by Gratzel, (2003), represent a great future. Nevertheless, this has inhibited the popularization of the technology considering the use of a liquid electrolyte. In case of highly improving the efficiency of the crystalline silicon solar cells, their usage in the tandem and multi-junction solar cells is essential. According to the Shockley-Queisser limit, the efficiency of a single-junction solar cell is 33%, and that of a tandem solar cell is 44% at global conditions (AM 1.5G) regardless of how many junctions are used. The

efficiency of the current-day single junction perovskite solar cell in 2024 has risen beyond the Shockley-Queisser limit when it reaches a record of efficiency of 34.6% in the records of research by Longi in 2024. This necessitates therefore, development of tandem solar cells using large band gap materials as the top cell and the bottom cell uses crystalline silicon. Top cell with this configuration is able to detect photons of greater energy yet pass lower energy photons to the bottom cell.

Perovskites have attracted a lot of attention and are a promising way forward to push the solar cell technology. They have outstanding absorption capabilities, modest charge carrier mobilities, carrier diffusion lengths that are large, shallow defect levels and direct band gap, leading to efficiencies as high as 25.8% They also permits variable tuning of band gaps within the materials (perovskite) by composition, which enabled flexibility in the uses of solar cells. They are however vulnerable to degradation under moisture, light, and heat in a long term and this is an issue to be solved to have them widely adopted.

1.2 Statement of the Problem

Even though the present optoelectronic performance of the methylammonium lead iodide ($MAPbI_3$) perovskite solar cells have been extremely promising, it has been discovered as extremely challenging to productively provide stable, ultra-crystalline, and morphologically well-optimized thin film materials. Native defects such as small grain sizes, varied morphology and increased concentration of defects lead to the non-radiative recombination and poor conversion efficiencies. The problem of incompatibility between optical and electrical is also there like the effects of hysteresis and the factors of interface losses which continue to affect the stability and the reproducing capability of the device.

Specifically, the effect of the operating parameters of fabrication, such as the annealing sensor, solvent engineering, and spin-coating procedures, on microstructure and the optoelectronic performance of the film deserve closer examination. Theoretically $MAPbI_3$ has a direct band gap near 1.52 eV and large absorption coefficients, but the real efficiency of a device is influenced by the grain boundary density, crystallinity, and film thickness.

This study responds to these issues by relating the structural, morphological, optical and electrical properties of $MAPbI_3$ thin films prepared by using a two-step annealing technique and rapid spin coating. The work seeks to optimize the film quality, gain knowledge about microstructural evolution and reduce hysteresis in $MAPbI_3$ -based planar perovskite solar cells using a combination of XRD, SEM image segmentation, UV -Vis spectroscopy, as well as J-V characterization methods, and minimize hysteresis in $MAPbI_3$-based planar perovskite solar cells.

1.3 Objectives of the Study

1.3.1 General Objective

The main aim of the study is to investigate the optical, electrical, structural and morphological properties of Methylammonium Lead Iodide and relate its performance in the complete solar cell.

1.3.2 Specific Objectives

i. To obtain the phase structure of $MAPbI_3$ perovskite films using X-ray Diffraction measurements.
ii. To compute the grain sizes and thickness of the $MAPbI_3$ perovskite films from the morphological images in the scanning electron microscope

iii. To determine the absorption coefficient and Tauc gap of $MAPbI_3$-based perovskites from UV-Vis spectroscopy.

iv. To evaluate the photovoltaic parameters of complete $MAPbI_3$ perovskite solar cell

1.4 Significance of the Study

The significance of this research is that it is able to advance the state of solar cell technology by advancing Methylammonium-based perovskites as absorber material by means of a thorough study and subsequent improvement. By comparing the properties and utility of these materials, the research will be of great help to generate understandings that can be used to make the solar cells perform better, be more stable, and more effective. The study can provide new horizons in the future enhancement of the conversion of solar power by better materials and optimization methods, thus developing sustainable energy in years to come.

1.5 Justification of the Study

The study present useful information which will assist in developing better solar cell devices by demonstrating considerable interest in optical and electrical properties of $MAPbI_3$-based perovskites. These two standout properties are important to understand and ideally use to the best of their ability and enable the further improvement of the solar cell technology by creating both more efficient and stable $MAPbI_3$ perovskites-based cells in the years to come.

CHAPTER TWO

LITERATURE REVIEW

2.1 $MAPbI_3$ as a Potential Material for Photovoltaic Applications

The perovskite solar cells based on Methylammonium lead iodide ($MAPbI_3$) have gained much interest in the photovoltaic industry because of their high performance and affordable production technique. This section plunges into the detailed examination of experimental research and optimization studies done on $MAPbI_3$-based perovskites as resorts of solar cell absorbers.

An in-depth review of the progress of $MAPbI_3$-based solar cells, which focuses on the relevance of determining the optical and electrical behavior of said materials, has been actively carried out to improve cell efficiency (Tonui *et al*.2020). Conversely, the studies have centered on how to best deposit MAPbI3 perovskite films so as to result into high-quality thin film with uniform thickness that is essential in enhancing the optical and electrical characteristics of solar cells (Lee *et al*. 2015). Additional focus depending on the relevance concerning the quality of films has been arranged in order to have high-performance $MAPbI_3$ based solar cells (Yang *et al*. 2017).

The experiment of UV-Vis spectroscopy analysis has shown the applicability of tunable band gap and high light-absorption ability of $MAPbI_3$ perovskites in a solar cell device (Kim *et al*. 2018). On the other hand, a sufficient study on the effect of charge transport and carrier dynamics in $MAPbI_3$ perovskite films has been carried out using transient

spectroscopy and impedance spectroscopy and lends knowledge about the recombination process (Chen *et al*. 2019) and transport of charges that affect the device performance.

Current studies on the study of $MAPbI_3$ perovskite solar cell degradation and stability under different environmental conditions showed deposits on the elements affecting performance and reliability over time (Wang *et al*. 2021). These investigations demonstrate the decisive importance of sufficiently studying the optical and electrical characteristics of $MAPbI_3$ perovskites to continue the progress of efficient and steady solar cells technology.

2.1.2 Properties of $MAPbI_3$ Perovskites

Perovskites $MAPbI_3$ are well-suited perovskites to be used in solar cells because of their distinct characteristics. The presence of a tunable bandgap is among the main benefits of $MAPbI_3$ perovskites since it enables such materials to capture the maximum amount of sunlight with a variety of solar wavelengths (Stranks and Snaith, 2015). Such property, in combination with the high charge carrier mobility can help to achieve high efficiency of $MAPbI_3$ -based perovskite solar cells.

In most cases, the Methylammonium lead halide perovskite materials are popular since they are easy to prepare and cheap at the same time. Yet perovskite materials have natural properties which include fast charge separation, long carrier separation lifetimes, long electron and hole transport lengths, wide-range absorption spectrum, high defect tolerance etc. This makes them very promising materials in the next-generation solar cells.

2.1.3 The Structure of Perovskites

The structure of perovskite is very similar to a known mineral known as calcium titanate ($CaTiO_3$) that was discovered by Tsutomu Miyasaka in 2009 (Kojima *et al*.,2009). The organic molecules present in the perovskites provide the natural material with a property of turning solar energy into electricity with no additional mechanisms like the use of doping as is the case with the silicon-based solar cells. A group of structurally correlated materials known as Perovskites have a general structure designation of ABX_3 where A, B, and X denote monovalent atomic organic cation such as Methylammonium ($NH_3CH_3^+$), Formamidinium ($NH{=}CHNH_2^+$(FA)); inorganic divalent metal cation as Pb^{2+}, Mg^{2+}, Sn^{2+}, or Sr^{2+}, and halide anion like Br^- or I^-, respectively (Kalyanasundaram, 2016).

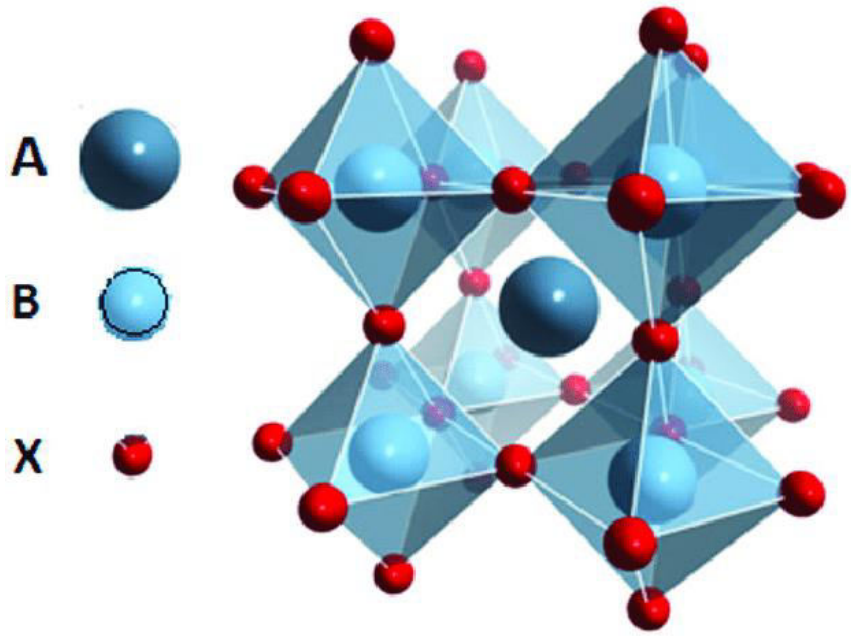

***Figure 2. 1**: Ideal ABX_3 structure of a perovskite*

(Masood, 2020)

The crystal can be represented by cube with an atom of type A in each corner, all cube corners occupied with atom of type B (Frost and Walsh, 2016) and an atom type X in each of the cube faces. The structure shape of the perovskite is dependent on size of the monovalent cation A and this feature assists in the stabilization of the charge within the lattice and it has little to no effect on the electronic character of the perovskite.

The pure $MAPbI_3$ crystal structure can be termed as perovskite in the following views: Octahedral coordination, by this it means that the PbI_2^+ are placed at the corner of an octahedron, comprising of 6-iodine ions. This structure is octahedral where the lead ions combine with the iodide ions; the presence of lead ions as octahedra promotes the structural stable nature of $MAPbI_3$; the Methylammonium cations ($CH_3NH_3^+$) in this case are located in the interstitial sites between the octahedra of lead iodide. These organic cations are especially important in stabilizing (Chen *et al*., 2015) the crystalline structure by hydrogen bonding interaction with the surrounding iodide ions, and ultimately the perovskite skeleton, where an arrangement of PbI_2 octahedra and $CH_3NH_3^+$ forms a three-dimensional perovskite structure with certain crystallographic symmetry and unit cell parameters. However pure $MAPbI_3$ usually has a cubic crystal structure, which is described by a characteristic lattice parameter that defines the distance between atoms in the substance.

2.2 The Fundamental Operation of Perovskite-based Solar Panels

It is necessary to consider the construction of perovskite solar cells (PSCs) because this is the way to achieve efficient light-to-energy conversion that PSCs have demonstrated regularly since their inception. Although the efficiencies of PSCs have increased rapidly to over 25 %, there remains limited knowledge of the fundamental photo physics,

principally of charging and trapping the electrons present in PSCs when compared to conventional silicon-based solar cells (Green *et al*., 2022). The latest studies mention that despite the advances, essential features of charge carrier dynamics, e.g., extraction, recombination and motion at interfaces, remain not well understood and highly susceptible to layout and material choices (You *et al*., 2023).

The solar cells have this perovskite material as an absorber layer called methylammonium lead iodide (MAPbI 3) or any other similar MAPbBr3, among other mixed-halide types, which are flanked by hole and electron transport layers on either side. The charges are extracted by the two different types of electrodes transparent and metallic kind (Snaith, 2022). The functioning of a perovskite solar cell occurs in three stages: (i) the absorption of the photons of light, separation into charges; (ii) separation of charges in the electric fields and energy level matching in the interfaces; (iii) the collection of charges, which is facilitated with the help of special electrical contacts (Shao *et al*., 2023). As an illustration, quick photocurrent determinations and photoluminescence yields demonstrate rapid photoinduced current flow implying fast and efficient driver translation in high-quality perovskite films (Wang *et al*., 2024).

The absorption of photons causes their energy to free the excitons (pair of electrons and holes) of the binding energies in the perovskite material. It is achieved by the separation of electrons and holes by movement of electrons to the electron transport layer and holes to the hole transport layer mediated by the built-in potential, thus allowing current flow through the circuit. The electrons and holes attract metal electrode contacts and force them to flow externally as an external load current.

2.3 Perovskite solar Cell Device Architecture

Traditional n-i-p devices tend to be constructed with TCO/ETL/Perovskite/HTL/Metal Electrode stack order. Electrons in this construction are transported by the glass layer and oxide film and gathered at the anode end whereas holes, by the metal top electrode, are collected and transported by PTAA, PEDOT: PSS, PCBM or Spiro-OMeTAD.

First this design was modeled after dye-sensitized solar cells and, now, high-record solar cell efficiency has been realized. In addition to this, TiO 2-based ETL materials must be heated past 450 0 C to complete and produce issues with flexible materials and processes that are both lower-cost and lower-temperature (You *et al*., 2023). Otherwise, conventional forms of structures tend to exhibit a high level of hysteresis that is caused by ion migration and stored charge at the boundaries (Chen *et al*., 2022).

Moreover, inverted (p-i-n) structure consists of the order of layers as follows: Perovskite, ETL, HTL, TCO and Metal Electrode. The holes are injected into the transparent bottom-electrode and through the HTL, whereas the electrons are released onto the top metal electrode via the ETL. Particularly, this set up is effective when combined with the ITO/PTAA/MAPI/C_{60}/BCP/Ag layer, as displayed in this study. The inverted configuration allows conducting lithography at temperatures below 150°C that correspond to non-rigid and polymeric substrates and roll-to-roll processes (Zhang *et al*., 2023).

P-i-n devices exhibit reduced current-voltage hysteresis compared to n-i-p devices because organic transports are used and because the interfacial contact is superior (Consumption Turn 2023). Water in the environment has a reduced chance of penetrating the material and the contact between the material and the metal is also secured due to the presence of the two additives (Wang *et al*., 2024).

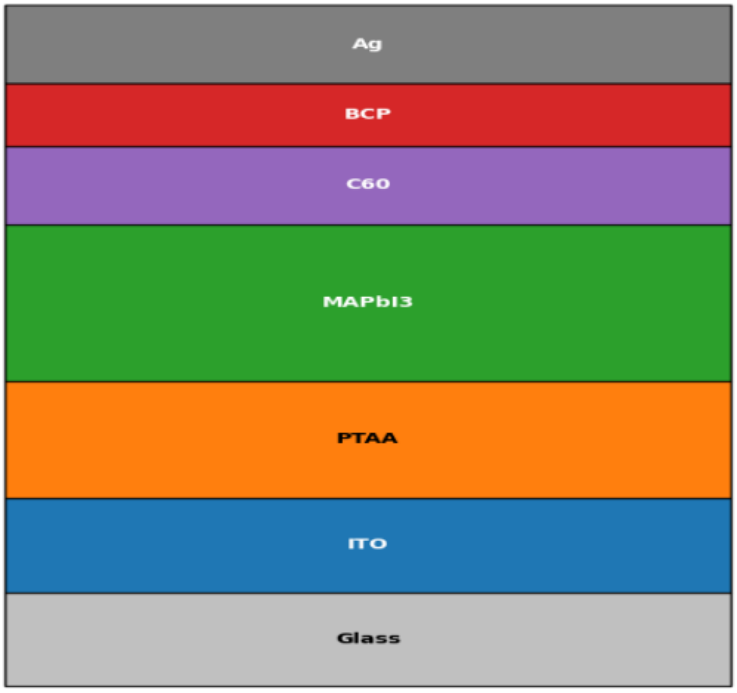

Figure 2. 2: Adopted Planar inverted Perovskite Architecture

The study was established on a planar inverted structure which has the following format; ITO/PTAA/$MAPbI_3$ /C_{60}/BCP/Ag with basis on the high-power generation, low hysteretic effects, and high stability. The transparent conductive oxide and anode layer is the indium tin oxide (ITO) layer through which the light enters the device. ITO is selected due to its good optical transmittances and low electrical resistances which makes them most appropriate to be utilized in the photo-voltaic cells that are front illuminated (Yin *et al*., 2023).

Finally, on top of ITO is hole transport material (HTM), poly [bis(4-phenyl) (2,4,6-trimethylphenyl) amine] (PTAA). The PTAA is chosen because it has good thermal stability, eco-friendly, wide energy range, and level of energy approaching valence band of the crystal perovskite. Also, it has a hydrophobic quality, which increases device stability by blocking the outside moisture on the perovskite layer (Wang *et al*., 2022).

The central component of the device is a perovskite absorber layer which is commonly methylammonium lead iodide ($MAPbI_3$). $MAPbI_3$ is quite appropriate in solar energy applications because of its direct bandgap, large absorption coefficient ($>10^4 cm^{-1}$) as well as long carrier diffusion lengths. On absorption of a photon, the excitons are created and immediately separated into free holes and electrons because of their small binding energy.

The electron transport material (ETM) is on top of the perovskite layer, and the ETM is C_{60}. C_{60} allows efficient collection of photo-generated electrons and holes are blocked concomitantly, considerably decreasing electron-hole recombination and lowering resulting losses. Its solution processability and the energy compatibility with the conduction band of $MAPbI_3$ result in its common utilization as an ETM in the inverted perovskite solar cell design (Min *et al*., 2017).

Better charge capture and enhanced strong steadiness at the interface is achieved by introducing a film of Bathocuproine (BCP) between the C_{60} and the metal. BCP isolates the interface, creates a wall and prevents the uncontrolled reaction of fullerenes with prime electrode layer. Moreover, the BCP layers are superb in reducing the number of recombinations that exist at the back contact (Rath *et al*., 2017).

The fabrication of the devices is finalized by the silver (Ag) top electrode, which acts as the cathode. There is the choice of silver because of the appropriate work function, ohmic contact to the ETM, and chemical inertness to the components in the device. These qualities make the device performance reliable, especially when applied in laboratory scale (Yang *et al*. (2020).

2.4 Solar Photovoltaic Performance Evaluation Parameters

Several input and output variables play a role in the process of solar energy conversion into an electrical power by a solar panel. Short-circuit current density (J_{sc}), Open circuit voltage (V_{oc}), Peak power (P_{max}), Fill factor (FF) and Power conversion efficiency (PCE) are the key determining factors to determine the efficiency of a solar cell (Ndiaye *et al*., 2014). Such parameters are measured on the basis of illuminated I-V characteristic curve as shown in Figure 2.3.

i. Short Circuit Current (I_{sc})

It is the current which passes through the cell to the external circuit in case of the short circuiting of the terminals of connection. This current is contingent upon photon flux of the incident solar radiation to the surface of the solar cell and strongly reliant upon the spectrum of incident light.

$$I_{sc} = J_{sc}A \qquad 2.1$$

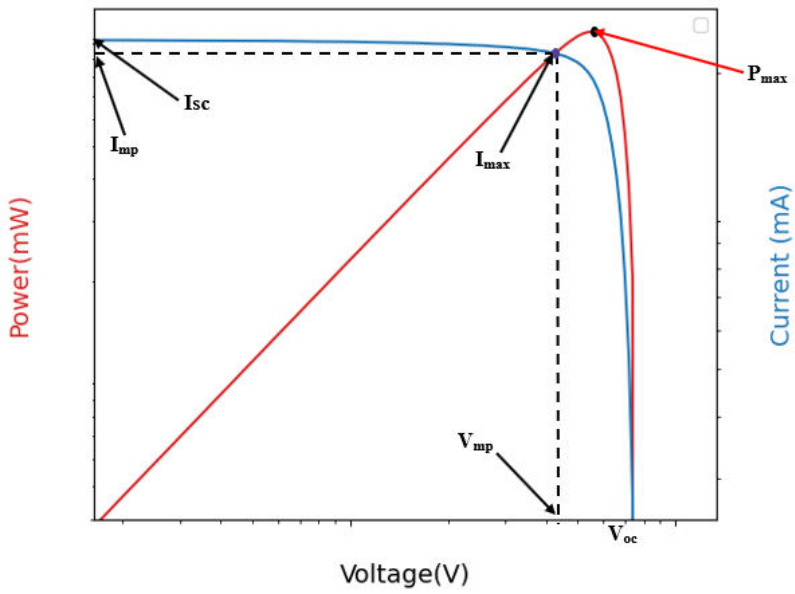

Figure 2. 3: *Typical I-V and P-V Curve for a solar cell device*

ii. **Short circuit current density (J_{sc})**

The parameter describes the highest current produced by the solar cell and is very dependent upon optical parameters such as reflectance and absorbance of the solar cell material. Short circuit Current density is simply the ratio of the short circuit current and the solar cell area.

$$J_{SC} = \frac{I_{sc}}{A} \qquad 2.2$$

iii. Open circuit voltage (V_{oc})

It is the highest value of voltage that a solar cell can supply in open circuit conditions. This parameter is influenced by the operating temperature; and the structure of the solar cell material. It is expressed in the form of the equation (2.3) below.

$$V_{oc} = \frac{K_B T}{q} \ln\left(\frac{J_{ph}}{J_0} + 1\right) \approx \frac{K_B T}{q}\left(\frac{J_{ph}}{J_0}\right) \qquad 2.3$$

iv. Fill Factor (FF)

This parameter is a representation of an I-V characteristic curve of the solar cell under consideration, which represents the squareness. It is the ratio between the maximum power output to the products of V_{oc} and J_{sc}. In mathematic form FF is written as;

$$FF = \frac{J_{mpp} V_{mpp}}{I_{sc} V_{oc}} \qquad 2.4$$

v. Power conversion efficiency (PCE)

This is the ratio of the power input to power generated in electrical terms as a percentage (%).

$$\eta = \frac{P_{\max}}{I_{in}} = \frac{J_{mpp}V_{mpp}}{I_{in}} \approx \frac{J_c V_{oc} FF}{I_{in}} \qquad 2.5$$

A typical I-V curve is read at standard test conditions (STC) that are 25ºC temperature, 1000 W/m^2 irradiance, and Air Mass 1.5 global (AM 1.5G). These conditions are in line with the standards proposed by American Society for Testing of Materials (ASTM).).

2.5 The Solar Spectrum

Photoactive materials in solar photovoltaic cells depend heavily on the solar spectrum in designing and optimization. An examination of the interaction of these materials with the various wavelengths of light comprising the solar spectrum can allow researchers to construct more effective solar cells that can convert the sunlight to electricity greater than before. The spectrum will normally be classified to 3 ranges as ultraviolet (UV) and visible light (Vis), which ranges between 4.4 eV and 1.6 eV and infrared (IR) that ranges between 1.6 eV and 0.89 eV. The section of the visible range, i.e., between 400 and 700 nm, is of particular importance since it constitutes around 43 percent of the solar energy that reaches the Earth (Jones & Lee, 2023). Majority of conventional solar cells, especially silicon-based, can absorb mainly visible light and a portion of the infrared range (Green *et al*., 2023).

However, of late, there is the emergence of perovskite-based solar cells because of their outstanding capacity of light absorption over extended solar spectrum both UV and

visible. It is because the band gap in these materials will be used to tune them to increase their efficiency and the specific wavelengths which they are capable of absorbing (Smith *et al*., 2023).

Moreover, novel methods of sunlight absorption with new technologies such as organic Photovoltaics (OPVs) and quantum dot solar cells are highlighted. OPVs also have organic materials that have the possibility of being customized to absorb wavelengths and the properties can be flexible and even have the possibility of lowering costs (Miller, 2023). Using Nanoscale materials such as quantum dot solar cells can be engineered to absorb light over a broad spectrum including into the infrared. This possibility creates the potential to design multi-junction solar cells that have the potential to capture more energy in the form of sunlight (Anderson *et al*., 2023).

Efficient use of a solar cell does not only depend on the light absorption but also on the capacity of the excited electrons (excitons) to be separated and led to the two electrodes of the cell (called excitons). It is a significant point in optimizing the effect of energy conversion (Lee *et al*., 2023). In general, the combination of photoactive materials and solar spectrum plays an essential role in the solar technology development.

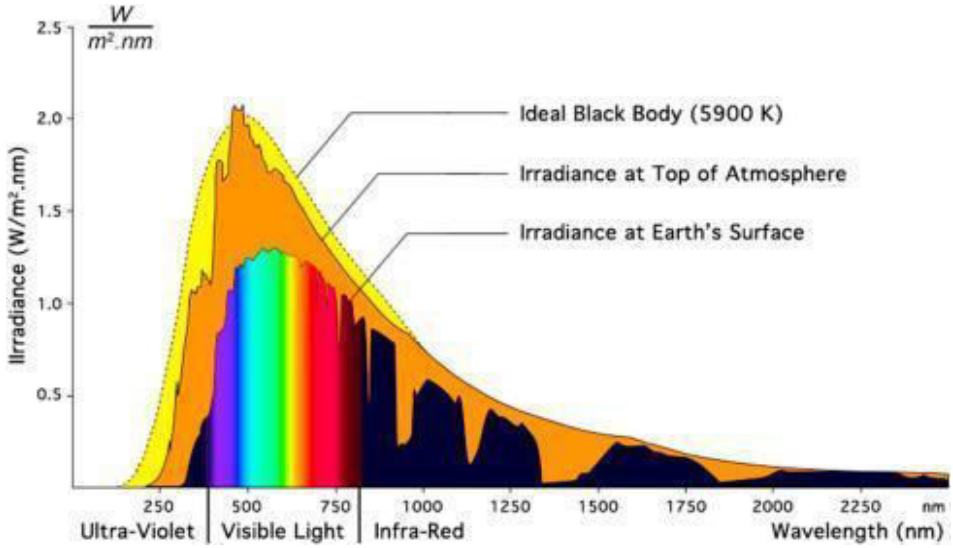

Figure 2. 4: *The Solar Spectrum*

(Wang *et al*.,2023)

Effective design of photovoltaic devices that enables the incorporation of absorber materials which have a different band gap energy is of essence in producing high-performance multi-junction devices with the ability to match the solar spectrum. Customization of multi-junction solar cells is one of the ways to reach high efficiencies and in such a case, specific layers of absorber insulate the various parts of the solar range. The method allows multi-junction solar cells to reach an efficiency of more than the single-junction technology achieves.

The American society of testing material (ASTM) controls the practice of the standardization of solar irradiance. When describing the solar irradiance that the earth gets on its surface, the standard used is ASTM-173-03 which is known as AM 1.5G and is defined as the hemispherical global irradiance, which encompasses the two direct and diffuse reflections. The standard is widely applied and normalized to an integrated power

density of 1000 Wm -2, using which solar cell calibration and characterization commonly take place (Stratford, 2016).

2.6 Charge Transporting Mechanisms in PSCs

The key parameters determining the nature of charge transport at the interface of the material include electronic energies like work function (Φ), Fermi levels (E_F), the vacuum level (E_{vac}), ionization energy (I_E) and activation energy (A_E). Such electronic states are very closely connected with the structure, shape, and chemical composition of a material. Work functions and vacuum level position can be drastically changed even by a slight quantity of impurities on the metal or semiconductor surface (Khan, 2016).

A work function (Φ) can be defined as the minimum energy needed to move an electron present at a point EF which is deep within the substance to a point which is the vacuum level E_{vac} (Khan, 2016). When talking about a metal surface, Φ is the difference between the Fermi energy (E_F) and vacuum level (E_{vac}). The difference in energy between E_F and E_{vac} is equal to Φ; it is similar to the difference between ionization energy (I_E) and electron affinity (E_A) of a metallic material. The ionization energy (I_E) measures the quantity of energy required to be used so as to free an electron at zero temperature (0 kelvin). In case of a molecule, I_E refers to the normal entropy of ionization at 0 kelvin temperature (Lang and Smith, 2003).

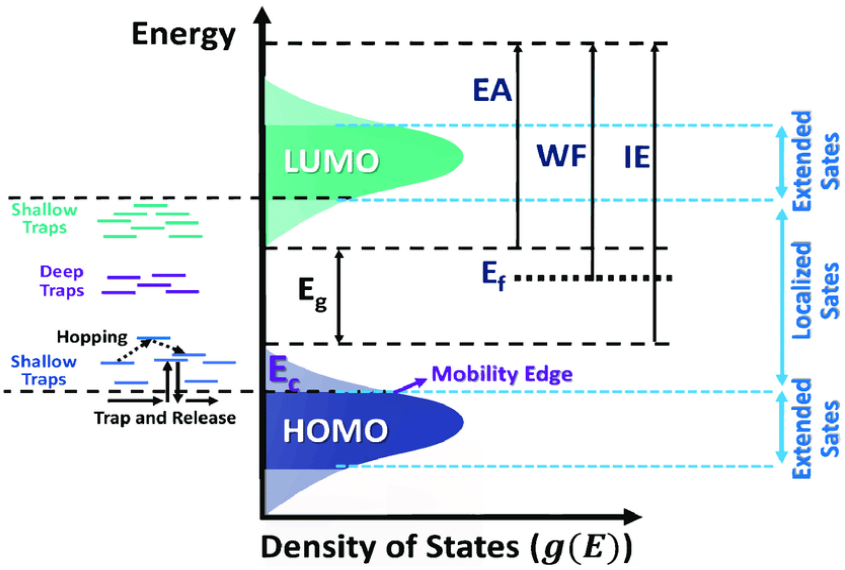

Figure 2. 5*: Schematic of a typical energy level diagram*

(Heydari *et al*., 2022)

In inorganic semiconductors, the work function (Φ) (WF) is a direct function of the Fermi energy (EF) and position of the vacuum level (E_{vac}) as given by:

$$\Phi = E_{vac} - E_F \qquad 2.6$$

Ionization energy, denoted as I_E, can be expressed as the difference between the vacuum (vacuo) level (E_{vac}) and the valence band energy (E_V), whereas the electron affinity (E_A) is related to E_{vac} and the conduction band energy (E_c) following the formula: $E_A = E_{vac} - E_c$. The band gap energy (Eg) is defined as the discrepancy between the energy levels of the conduction band minimum (E_c) and valence band maximum (E_v), represented as $Eg = E_c - E_v$. In organic semiconductors, the energy levels are characterized by the highest occupied molecular orbital (HOMO) and lowest unoccupied molecular orbital (LUMO) for a neutral molecule in its ground state. Theenergy difference between the LUMO and the HOMO levels is related tothe band gap (Eg).

Role of workfunction of electron and hole transport layers is important in device performance especially the workfunction of electron and hole transport layers. perovskite-based solar cells open circuit voltage (Voc). Studies have shown that Voc of a typical (n-i-p) structure is much larger than that of an inverted

This is because the (p-i-n) structure is designed to work with (Zhang *et al* ,2021). Oxides of inorganic metals which are used as electron selective materials (ETM) have large band gaps. For example, the band gap of SnO2 (3.5 eV) is significantly high. ETMs can absorb higher-energy photons using these wideband gaps without adding anything.

considerably to photocurrent so as to minimize current losses caused by the ETM (electron transport layer).

2.7 Absorption coefficient

The rate of decrease in the intensity of light whilst traversing a material is called the absorption coefficient (alpha) which is the fraction of light per unit thickness of the material (Pankove, 1975). Recent developments in material science have shown that several types of ultra-thin photovoltaic materials are able to reach very high absorption coefficients (>104 cm -1) in the visible range and thus allow sub-100 nm active layers without sacrificing the light harvesting efficiency (2D perovskites, Jiang *et al*., 2023; organic-inorganic hybrids, Wang *et al*., 2024). This property is of especially high importance in the next-generation photovoltaics where the minimization of material consumption should be weighed against the optical performance (NREL Technical Report, 2023). Researchers have emphasized that the absorption coefficients (alpha; 2) is

the critical parameter to attain high performance in perovskite solar cells mainly because it has a high absorption in the visible range of light (Jeon *et al*., 2021). In addition, it is important to tune the absorption coefficient via molecular engineering in organic photovoltaic devices (OPVs) to improve device efficiency (Li *et al*., 2022). The absorption coefficient value is usually determined with the help of optical instruments like UV-Vis spectrophotometers. The most common method is to measure absorbance (A), transmittance (T) and reflectance (R) of a thin film most of the time

The parameter can be calculated using the data of the absorbance as long as the thickness of the film is known according to Beer-Lambert equation:

$$A = \alpha \cdot d \qquad 2.7$$

with d the thickness of the film. However, in the case of thin films special consideration should be paid to reflection losses and interference. To be able to express better, reflectance (R) (Pankove, 1975) and transmittance (T) should be written as:

$$\alpha = \frac{1}{d} ln \left(\frac{(1-R)^2}{T} \right) \qquad 2.8$$

2.8 Tauc gap

The Tauc gap is an optical measurement of the band gap energy (Eg) of semiconductors, especially amorphous, thin film and nanostructured materials, introduced in 1966 by Tauc, Grigorovici and Vancu. The Tauc method, based on optical absorption measurements, has gained popularity in materials science, optoelectronics and photonics.

The electronic and optical properties of semiconductors are basic in determining the Tauc gap. It gives an understanding of the interaction of materials with light, which is necessary

in the rational design of solar cells, photodetectors, and photocatalysts (Green *et al*., 2022). It also provides a way of measuring the extent of disorder in amorphous materials and to customize the absorption edge to a particular purpose.

The procedure entails the analysis of the absorption coefficient (alpha) derived through optical spectroscopy-usually UV-Vis. Tauc gap is mathematically represented as

$$(\alpha h\nu)^{n} = A\,(h\nu - E_g) \qquad 2.9$$

where hv is the energy of the photon, A is a constant, Eg is the bandgap and n is dependent on the type of transition (n = 1/2 in direct transition band gaps and n = 2 in indirect band gaps).

A graph of (alpha hnu) n versus hnu is plotted and the linear part of the graph is extended to the energy axis. The Tauc band gap is shown by the intercept. This graphical technique is very common to estimate both direct and indirect band gap, particularly in thin films and nanomaterials (Griffiths & de Haseth, 2007).

In the latest research, researchers have utilized Tauc analysis in numerous material systems to correct and interpret their optical band gaps. Patra *et al*. (2023) state that ZnO nanoparticles exhibit a greater band gap as a result of quantum confinement. This implies that nanomaterial engineers can apply the Tauc gap to enhance the structure of their materials in a better way. Amorphous titanium dioxide (TiO 2) thin films were also examined through the Tauc method and it was revealed that optical transitions were highly dependent on film preparation. It established the fact that the method was able to identify subtle variations of disordered materials due to structure.

Hou *et al*. (2021) used the Tauc analysis to study the influence of molecular ordering on the optical band gap in organic solar cells in organic and hybrid photovoltaics. The work demonstrated that microstructural variations may influence the efficiency of charge production and once again demonstrated the utility of the Tauc technique in the development of advanced optoelectronic devices. Also, Zhang *et al*. (2020) discussed the application of Tauc plots in the process of choosing photocatalysts that require required band gaps, which are beneficial in energy applications, as well as environmental applications such as water splitting and the removal of pollutants. In general, they show that Tauc method is still useful and meaningful in contemporary materials study.

2.9 Characterization Techniques for Perovskites

The perovskite materials and devices need a full understanding to comprehend. the way their properties vary and how they can be optimized and made more stable by means of their structure improvement. The probing is done using various tools that concentrate on various aspects like crystal structure, shape, optical properties and electrical properties of perovskite films.

2.9.1 X Ray Diffraction (XRD) Technique

X-ray diffraction (XRD) is a non-destructive method that allows determining the crystal structure, orientation, and phase purity of perovskite thin film. XRD can be used to determine the particular phase of perovskite, e.g., methylammonium lead iodide (MAPbI 3) by exposing the atomic arrangement in the crystal lattice. In line with the literature, MAPbI 3 normally crystallizes in the tetragonal structure, and in this case, it has two specific diffraction peaks at $2\theta \approx 14.1°$ and 28.3°, which are attributed to the (110) and (220) lattice planes, respectively (Stoumpos *et al*., 2013; Yin *et al*., 2023; Jeon *et al*., 2015;

Niu *et al*., 2021). The existence of high sharp and intense peaks is indicative of high crystallinity that is closely related to high performance of the device.

X-ray diffraction, XRD, uses a principle known as Bragg Law (Stock, 2001) that is used to relate diffraction angle and lattice spacing between two crystals.

$$n\lambda = 2dsin\ \theta \qquad 2.9$$

N = 1 is the diffraction order, 2 is the wavelength of the λ -rays, d is the interplanar spacing and 2 is the angle of diffraction. Using this relationship-Bragg-s Law, diffraction peaks can be indexed and different crystal planes differentiated.

Moreover, the average size of crystallites in the perovskite films can be quantitatively determined with the help of the Scherrer equation (Scherrer, 1918; Jeon *et al* 2014)..

$$D = \frac{K\lambda}{\beta cos\ \theta} \qquad 2.10$$

and where: D is the crystallite size, K is the true value of the shape factor (this is normally 0.9). An example of a common X-ray wavelength of 1.5406 A (Cu K alpha radiation) symbolized by the symbol . The full width at half maximum (FWHM) of a diffraction peak, 2 (in radians) is a measure of the peak broadening about the Bragg angle. Based on the equation, the assumption is that the broadening of the peaks is mainly due to the finite size of the crystallites and not due to the lattice strain or the instrumentation. This method is then used to estimate the mean size of coherent scattering domains, which is usually the

grain size, and is important to know in relation to the optoelectronic properties of the perovskite layer (Turren-Cruz *et al*., 2018; Kim *et al*., 2021).

Also, the presence of lead iodide (PbI 2) can be observed by X-ray diffraction (XRD) and usually a peak is observed at $2\theta \approx 12.7°$. This stage can be prolonged because of the lack of conversion of the precursors or can be formed as a degradation product (Wei *et al*., 2022; Kim *et al*., 2020). The process of monitoring such features helps to optimize the process and continuously assess the stability of the film. As a result, XRD, as the instrument based on the principles developed by Bragg and Scherrer, is an essential structural analysis instrument in the study of perovskite solar cells.

2.9.2 Scanning Electron Microscopy (SEM)

SEM gives a detailed information on the surface and cross-sectional morphology of perovskite films. The main characteristics that are identified are grain size, uniformity of coverage, and thickness of the film; which affect the charge transport and recombination in PSCs. As an example, larger grains and the smaller number of grain boundaries are usually associated with the lower trap-assisted recombination and the increased carrier diffusion lengths (Chen *et al*., 2022). In planar inverted devices, cross-sectional SEM is particularly valuable in seeing the layer stack and uniformity of thickness through the stack.

Image segmentation in materials science assists in obtaining numbers in the images obtained with the help of microscopes. SEM images of perovskite solar cells are segmented using image segmentation to identify the grain size distribution, the uniformity of the film, identify any voids and the thickness of the film. The structure of perovskite

films should be examined closely because it influences the electrical charge transport, charge carrier interactions and the functionality of the entire device (Li *et al*., 2023).

The segmentation of the image allows locating single grains or features and measuring it off all the others in the image. The most important parameters of morphology affecting the quality of perovskite films are the average grain size, particle size distribution, surface coverage, grain compaction and cross-section thickness. Bigger and more evenly dispersed grains lead to a smaller number of grain boundaries and less recombination sites, which allows more efficient charge transport and, eventually, higher device performance (Zhao *et al*., 2021).

Before analysis, SEM images are usually preprocessed by noise reduction and contrast enhancement via filters, e.g. Gaussian or median filters. The segmentation of grain is then carried out using thresholding methods, and the most common ones are Otsu method and adaptive thresholding (Yao *et al*., 2020). In order to identify grain boundaries, edge detection algorithms like Sobel, Canny or Laplacian filters are used.

In segmentation, a number of techniques are used to isolate individual grains-particularly those in contact. This is often done through watershed segmentation. Intensity-based classification methods such as K-means clustering, region-growing algorithms and grain-shape-based active contour models are other methods. Segmentation of more complex/low-contrast images, e.g. medical imaging, can be done using deep learning-based segmentation methods, e.g. U-Net and convolutional neural networks (CNNs) (Shan *et al*., 2022).Once the image has been segmented, each region can be labelled, and important morphological characteristics, such as area, perimeter, and orientation, can be

extracted using software packages, e.g. OpenCV, ImageJ, or the Image Processing Toolbox in MATLAB.

The recent works have revealed the applicability of these image segmentation methods to perovskite films. As an example, Yao *et al*. (2020) thresholded and morphologically filtered grain size distributions in MAPbI 3 thin films prepared using various solvents. In the meantime, Shan *et al*. (2022) applied deep learning to the segmentation of SEM images of perovskite grains and obtained useful information about grain morphology and film thickness. In the current work, the automated segmentation through the OpenCV was used to study the effect of annealing temperature on the grain growth.

2.9.3 UV-Vis Spectroscopy

UV-Vis spectroscopy is a standard tool to study the optical properties of perovskite materials, which are of interest to study the light absorption and optical properties, especially in materials like methylammonium lead iodide (MAPbI 3). Typical standard MAPbI 3 films have sharp absorption onset and wide absorption in the visible spectrum. Depending on the synthesis conditions, composition, and crystallinity, the optical bandgap is typically found in the range of 1.5-1.7 eV (Zhou *et al*., 2022; Sutter-Fella *et al*., 2023; Kim *et al*., 2021).

One of the important parameters obtained through UV-Vis data is the absorption coefficient (alpha) that measures the efficiency of the material to absorb light at various wavelengths. MAPbI 3 has a high absorption in the solar spectrum, and the 104 -105 cm -1 2 value is higher than 104 -105 cm -1 at the band edge (Tang *et al*., 2023; Peng *et al*., 2022).

Tauc plots are usually used to estimate optical bandgap. A graph of (alpha hnu) 2 versus photon energy (hnu) e.g. in direct allowed transition materials, such as MAPbI3, will have a linear region at or close to the excitation threshold. This linear section is then extrapolated along the energy axis to give this slope to approximate the energy of the bandgap (Zhou *et al*., 2022; Lin *et al*., 2023). Because the bandgap can be readily modified by the addition of secondary phases, grain size, composition, bandgap tuning, e.g. by addition of Br- or FA+, UV-Vis can be applied as a characterization method, and as a method of tracking the temporal evolution of a material.

CHAPTER THREE

MATERIALS AND METHODS

3.1. Materials

The materials required for the preparation of the $MAPbI_3$ thin film were: Methylammonium iodide (MAI), Lead iodide (PbI_2), Dimethylformamide (DMF) and Dimethyl Sulfoxide (DMSO) solvents, distilled water, detergent, Isopropanol, chlorobenzene anti-solvent, C_{60}, PTAA, Silver electrode, BCP, and ITO coated glass substrate.

3.2 Substrate Preparation

The ITO-coated glass substrate was precisely cut into 20mm by 15mm to fit in the spin coater sample holder using a standard glass cutter. It was then cleaned using deionized water for 15 minutes, acetone for 15 minutes, and finally in isopropanol in a sonicator (Elmasonic P 30 H, Serial number S1000053860) for 15 minutes to make a dust-free and contamination-free surface. The cleaned substrate was left to dry under nitrogen stream on the substrate holder for 25 minutes before deposition.

3.2.1 Perovskite Film Preparation

1M precursor of MAPI was prepared by mixing 158.97 mg (Chen *et al*,2015) of MAI (Methylammonium Iodide) and 461.01mg PbI_2 (Lead Iodide) which were weighed using a weighing balance inside a nitrogen-filled glovebox (TMAXCN, Model GBP800S-2) (Miller *et al* 2024). The precursor solution was prepared by dissolving 1 M MAI and 1 M PbI_2 in Dimethylformamide (DMF): Dimethyl sulfoxide (DMSO) solvent (6:1 v: v). The

precursor solution was then stirred using a magnetic stirrer overnight to obtain a clear and homogeneous solution.

The spin coater (Ossila Model) was set to spin in two sequential steps. Initially, it was set to spin at a controlled speed of 1000 rpm for a duration of 15 seconds and then 5000 rpm for 25 seconds to allow for the uniform dispersion of the coating across the substrate. A 0.22 μm polytetrafluoroethylene (PTFE) filter was used to filter the solution before deposition. 50μl of the precursor solution was then carefully dripped onto the center of the conducting side of the ITO substrate on the spin coater chuck. To enhance the integrity of the film during the coating process, 100 μl of chlorobenzene was dripped onto the substrate at exactly 5 seconds towards the end as the spinning progressed. This anti-solvent dripping serves a dual purpose by assisting vaporizing the solvents and thereby controls the viscosity of the coating solution and forms an encapsulating (capping) layer that acts as a moisture barrier which is very beneficial for preventing exposure to moisture while transferring the films from the glovebox.

The spin coater (Ossila Model) was adjusted to be spun within two steps. It was later programmed to rotate at a moderate pace of 1000 rpm and 25 seconds followed by 5000 rpm and 25 seconds so that the coating could be evenly spread along the substrate. The solution was filtered using a 0.22μm polytetrafluoroethylene (PTFE) filter before depositing. Using a pipette, 50μl of the precursor solution was placed at the center of the conducting surface of the ITO substrate on the spin coater chuck after which 100 μl of chlorobenzene was dripped directly at 5 seconds before the end of spinning. This anti-solvent dripping also performs two functions in that it helps vaporize the solvents and in turn regulates the viscosity of the coating solution and forms an encapsulating (capping)

layer which is a moisture barrier and is quite useful in preventing the exposure to moisture when transferring the films out of the glovebox.

The resultant MAPI film was annealed partially on hot plate (GUARDIANTM7000), at 100ºC, 10 minutes in a nitrogen- filled glovebox (TMAXCN, Model GBP800S-2). This regulated heating helped to remove any remaining solvent that may have a negative impact on the quality of the film when left in excess.

3.2.2 Perovskite Device Fabrication

The solar device was fabricated by adding layers in order one by one to indium tin oxide-coated glass, with the final structure being ITO/PTAA/$MAPbI_3$/C_{60}/BCP/Ag. The ITO substrates were first prepared by sonication in deionized water, detergent, acetone and isopropanol for 15 minutes each. The substrate surfaces were dried under a nitrogen stream after solvent cleaning and exposed to UV-Ozone treatment for 25 minutes to increase wetting of the surface and eliminate remaining organic contaminants which led to better adhesion of the subsequent coatings, according to Kim *et al*. (2019).

A 5 mg/ml solution of poly[{bis (4-phenyl) (2,4,6-trimethylphenyl) amine] (PTAA) was spun on top of chlorobenzene. The polymer solution was deposited by spin-coating at 5000 rpm and 30 seconds and annealed on a hotplate (GUARDIANTM7000) at 100oC during 10 minutes to obtain a uniform film (Jung *et al*., 2020).

The active layer of perovskite was subsequently deposited on the Hole Transport Material (PTAA) that was prepared by mixing 200l DMF, 78 µl of DMSO, 158.97 mg of MAI and 461.01mg of lead iodide (PbI_2). The mixture was stirred at night to obtain complete dissolving and homogeneity (Park *et al*., 2018). The solution was filtered through a 0.22

μm polytetrafluoroethylene (PTFE) filter prior to deposition. 5 seconds before the spin cycle was complete, A100 μL of chlorobenzene was added to the spinning substrate to evaporate the solvents. Immediately after the formation of the film, it was dried in air 5 min and placed in a hot plate (GUARDIANTM7000) and annealed at 100 ^{o}C for 10 min to further enhance the crystal structure and to make the film even (Liang *et al*., 2022). Then 20 nm of fullerene (C_{60}) material was deposited on the perovskite film by high vacuum (~10^{-6} Torr) thermal evaporation. This layer as ETM would enable efficient movement of electrons out of the perovskite absorber and also block surface traps (Chen *et al*., 2021). Then, the C_{60} layer received a thermal deposition of around 7 nm of bathocuproine (BCP). The BCP acted as a buffer layer and helped prevent defects and improved how charge moved to the top electrode (Zhou *et al.*, 2023).The structure was completed by thermally evaporating an 80 nm Silver (Ag) electrode under vacuum. The metal layer allowed the formation of good and uniform paths for hole collection and formed an ohmic link with the HTM. A UV-curing epoxy was applied, and a glass coverslip was introduced to ensure the devices would be stable in the environment and protected from both moisture and oxygen (Wang *et al*., 2021).

3.3 Characterization Techniques

3.3.1 X-ray Diffraction

The grazing incidence X-Ray diffraction pattern of thin films was measured using Bruker AXS (D8 Advance) equipment (Cu Kα radiation source, at wavelength 0.154065A, and 9-fold sample changer). The material was put into a path of the X-ray beam, and the incident X-rays struck the crystal lattice. The X-rays being incident on the crystal lattice plane are diffracted, leading to constructive interference at a certain angle of angle 2 theta

deposed on the lattice spacing (parameters) of the crystal. The detector recorded the diffracted X-rays and a diffraction pattern (XRD pattern) was measured, indicating the intensity of X-rays diffracted at various angles (2θ) between 10-70 degrees, with the scanning step size of 0.02° and an acquisition time of 4 seconds per degree. The XRD pattern peaks indicated the crystal planes and lattice spacing of the material; with each peak yielding data regarding the crystal structure and orientation of the sample. The analysis of the position of the peaks (2 angle) and the intensity of peaks was used to determine the crystal structure, phase composition, and orientation of the MAPI thin film.

3.3.2 Scanning Electron Microscopy (SEM)

The microstructure of the $MAPbI_3$ films with chlorobenzene anti-solvent treatment was examined using a high resolution scanning electron microscopy (SEM) (FEI/Thermo Scientific Quanta 600 FEG) under varied scale factors (magnification) ranging from 10,000X to 30,000X on the cross sections and top to determine the thickness and diameter of the film respectively at an accelerating voltage of 5kV, followed by image segmentation in python 3.12.7 software to quantify grain size and shape distribution of the fabricated device.

3.3.3 UV-Vis Spectroscopy

The optical analysis was carried out using a commercial UV-Vis spectrophotometer (Perkin Elmer Lambda 1050 model) whose spectral range was 175 nm to 3300 nm. The device included the source of light (which emits both ultraviolet and visible light) and a collector where the thin film is laid down as well as the detector that indicated the absorbance of the light or transmission. One of the detectors was a photomultiplier (PMT) combined with InGaAs working at the wavelength range of 860-1800 nm and a broad

band of 860-2500 nm. The second detector was PbS detector which had sensitivity at 1800/2500-3300nm.

The spectrophotometer emitted both ultraviolet and visible light to which the MAPI thin film sample was exposed and the detector measured the amount of light that was absorbed by thin film with respect to the wavelengths (400 nm-900 nm). To measure the light transmission through the thin film, the quantity of light transmitted through a thin film was measured as a variable parameter to determine the level of the absorption of light. Lastly, The UV-Vis spectrum was achieved, displaying absorbance or transmittance of light versus the wavelength. Obvious highs and falls in the plot are due to the characteristics of the absorption of the fabricated perovskite compound.

3.3.5 J-V Scan Photovoltaic Performance Analysis

Keithley Instruments Inc (Model 2400, 4053247, C32) source meter was connected to the fabricated MAPI thin film device with accurate test leads (probes) to provide established electrical contact between the device under test and source meter. Subsequently, the instrument unit was set up to undertake J-V scanning by setting the correct voltage and current range used to take the measurement. Compliance limits were fixed at 70 mA/cm^2 to shield the device under test. A voltage sweep was conducted on the MAPI thin film to initiate scanning at a fixed intensity of 100 mW/cm^2 in an active region of 0.16cm^2. It was pre-programmed to gradually vary the voltage between -0.1 V to -2.0V and measure the corresponding current at every level and then maintain the cell at that voltage state 50 ms prior to recording an I-V curve.

The current flowing through the MAPI thin film was measured at each voltage step of the scan with the Keithley Model 2400 source meter. To obtain more comprehensive data and to confirm the validity of electrical characterization of the MAPI thin film, the entire process of scanning in various directions (forward and reverse) was repeated in variations of setting four times. The device offered data points with the current-voltage characteristics. The python 3.12.7 was then used to map the data points acquired using the instrument.

3.4 Data Visualization and Analysis

The generated experimental data was mapped onto Python 3.12.7, which was installed within the Anaconda, Inc. (*www.anaconda.org)* environment, compatible with both Linux and Windows operating systems. Python is recognized as a high-level, open-source programming language that harmonizes the syntax of multiple programming languages, including MATLAB, C, C++, and JavaScript, which enhances its versatility in scientific computing. In the visualization and analysis activities, Matplotlib, Pandas, NumPy, SciPy, Scikit image and OpenCV modules were mostly used because of the high functionality and outstanding flexibility and accuracy in dealing with complex data representations.

Spyder integrated development environment (IDE) was preferred to other scripting tools such as Jupyter Notebook because it had an easy to use interface and powerful debugging capabilities that allowed errors in the code to be detected and corrected easily, simplifying the process of coding. Once the Python scripts of the different datasets were debugged properly, they were then run to allow visualization. The plots created made it easier to interpret the trends and nature of the experiment and formed the basis of the analysis where it was possible to make effective comparisons with the existing literature and gave good

insight into the data.. In addition to the Python-based analysis, Origin Lab 8.5 was employed to perform manual linear fitting for the output plots where precise value matching was critical for the experimental datasets. Origin Lab is renowned for its user-friendly interface, very close to that of an Excel spreadsheet, which simplifies the graphing and data analysis processes.

CHAPTER FOUR

RESULTS AND DISCUSSIONS

4.1 Structural Characteristics of $MAPbI_3$

Figure 4.1(a) displays the XRD diffraction pattern of $MAPbI_3$, showing intensity (a.u.) versus diffraction angle (2θ in degrees). Prominent diffraction peaks were labeled with their corresponding Miller indices: (110), (211), (202), (220), (310), (312), and (314**)**. The strongest peak at approximately 14.128° corresponds to the (110) plane, which is a characteristic signature of the tetragonal perovskite phase of MAPbI. These peak assignments are consistent with well-established reports on tetragonal $MAPbI_3$ perovskite structures: Stoumpos *et al*., (2013) described characteristic peaks at ~14° (110), 28° (220), and higher-order planes corresponding to the tetragonal structure (space group I4/mcm). Im *et al*., (2011) observed similar indexed peaks verifying the crystallographic identity and phase purity of $MAPbI_3$. The (110) orientation is advantageous for charge transport, as the Pb-I-Pb network along this direction facilitates high carrier mobility (>20 $cm^2\ V^{-1}\ s^{-1}$) (Stranks *et al*., 2013), consistent with the high fill factor (FF = 63.8%) observed in this study.

Figure 4.1(b) plots the calculated interplanar spacing (d-spacing, in Å) as a function of the diffraction angle (2θ). The relationship between 2θ and d-spacing follows Bragg's Law:

$$n\lambda = 2d\sin\theta \qquad 4.1$$

where: λ is the X-ray wavelength, θ is the Bragg's diffraction angle and d is the interplanar spacing.

The graph clearly shows a decreasing trend in d-spacing with increasing 2θ angle, indicating smaller interplanar distances at higher diffraction angles, consistent with Bragg's law. The results are comparable to those reported by Yin *et al*. (2015) who also observed decreasing d-spacings in perovskite materials as higher-order planes are probed.

Figure 4.1(c) explicitly presents the correlation between d-spacing and the labeled Miller indices. Clearly, there was progression from lower-order (110) planes toward higher-order indices such as (314), a progressive decrease in d-spacing, signifying tighter atomic packing in these crystallographic orientations. The notable decline in d-spacing from approximately 6.3 Å (110) to around 2.1 Å (314) confirms the crystal lattice planes expected hierarchical ordering in $MAPbI_3$. Lower-index planes (110, 211) have larger spacing reflecting fundamental lattice dimensions while higher-index planes (310, 312, 314) have smaller spacing, reflecting higher-angle planes with denser atomic arrangements. These findings were comparable to those reported by Park *et al*. (2015) who demonstrated decreasing lattice spacing with increasing Miller indices for $MAPbI_3$. Saliba *et al*. (2016) similarly confirmed the reported relation of Miller indices with lattice parameters in perovskite structures.

Figure 4.1(d) shows the Full Width at Half Maximum **(**FWHM**)** of selected peaks ((110), (220), and (310)) plotted against Miller indices. FWHM, measured in reciprocal space ($Å^{-1}$), provides critical information about crystal quality, grain size, and strain. Smaller FWHM (e.g., (110)) indicates larger crystallite domains, lower lattice strain, and better

crystallinity. Larger FWHM at higher Miller indices (220, 310) suggests smaller crystallite sizes, increased lattice strain, or imperfections at higher-order reflections. The increasing trend of FWHM with higher Miller indices is typically associated with reduced domain size or increased structural disorder at higher-order planes and implied that the films showed greater sensitivity to micro strain at these crystallographic orientations.

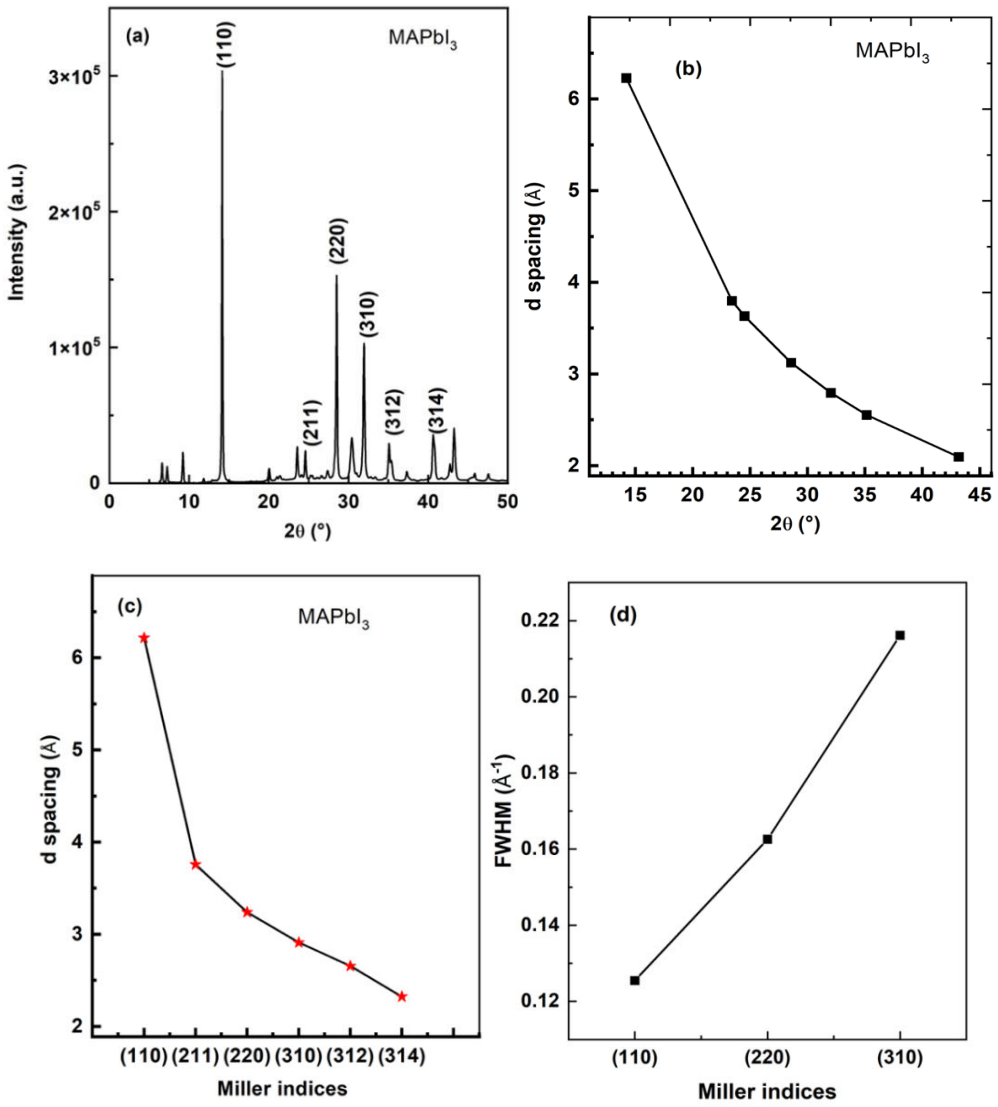

Figure 4. 1: X-ray Diffraction Pattern of $MAPbI_3$(a), lattice spacing for $MAPbI_3$ (b), d-spacing for corresponding miller indices (c) and FWHM vs three dominant miller indices (d)

4.2 Morphological Analysis

As shown in Figure 4.2(a), the SEM image depicts a dense and continuous film with a relatively uniform distribution of grains. A total of 314 grains were successfully identified and analyzed through automated segmentation (see Figure 4.2(a)).

The resulting size distribution histogram in Figure 4.2(c), shows that the average grain diameter is 196 ± 36 nm, with most grains falling within the 150-250 nm range. This size regime is considered optimal for planar perovskite solar cells, as it balances the need for strong light absorption with the requirement for efficient carrier diffusion. Prior studies have shown that grain sizes below 100 nm increase trap-assisted recombination due to a high density of grain boundaries (Stranks & Snaith, 2015), while excessively large grains (>500 nm) can result in non-uniform film coverage and poor interfacial contact (Zhao *et al*., 2023). Our results lie within the ideal range for minimizing recombination and optimizing charge transport.

Grain shape characteristics, including circularity and solidity, were further evaluated (Figure 4.2(d),). Most grains exhibited circularity values close to 1.0 and high solidity, exhibiting well-defined, compact morphologies with minimal edge roughness. These metrics reflect high crystalline quality and low morphological disorder, factors known to correlate with enhanced open-circuit voltage (Voc) and fill factor (FF) (Yang *et al*., 2017). A noticeable decrease in circularity and solidity was observed in grains exceeding 250 nm in diameter, suggesting minor aggregation or incomplete crystal boundaries: common in films without controlled crystallization steps.

The morphology is explained by the two-step annealing and anti-solvent engineering used in the fabrication of the film. The first annealing at 60 C helped in the removal of the

solvent and seed nucleation whereas the second at 100 C helped in full crystallization and phase formation. This strategy is consistent with the results of Kim *et al*. (2024), who proved that stepwise thermal processing increases the crystallinity of MAPbI 3 and inhibits non-radiative recombination. This work has a uniform grain size and morphology compared to single step annealing methods, which tend to produce wider size distributions and pinhole formation (Tonui *et al*., 2020). Also, high-speed spin coating (5000 rpm) and chlorobenzene as an anti-solvent were important in the control of nucleation kinetics and film thickness. Increasing the rotation rate increases the rate of solvent evaporation whereas controlled anti-solvent quenching allows the formation of uniform crystals and prevents uncontrolled grain growth. Similar benefits were reported by Lee *et al*. (2015), where chlorobenzene-assisted spin coating yielded compact $MAPbI_3$ layers with minimal surface defects and improved power conversion efficiency (PCE).

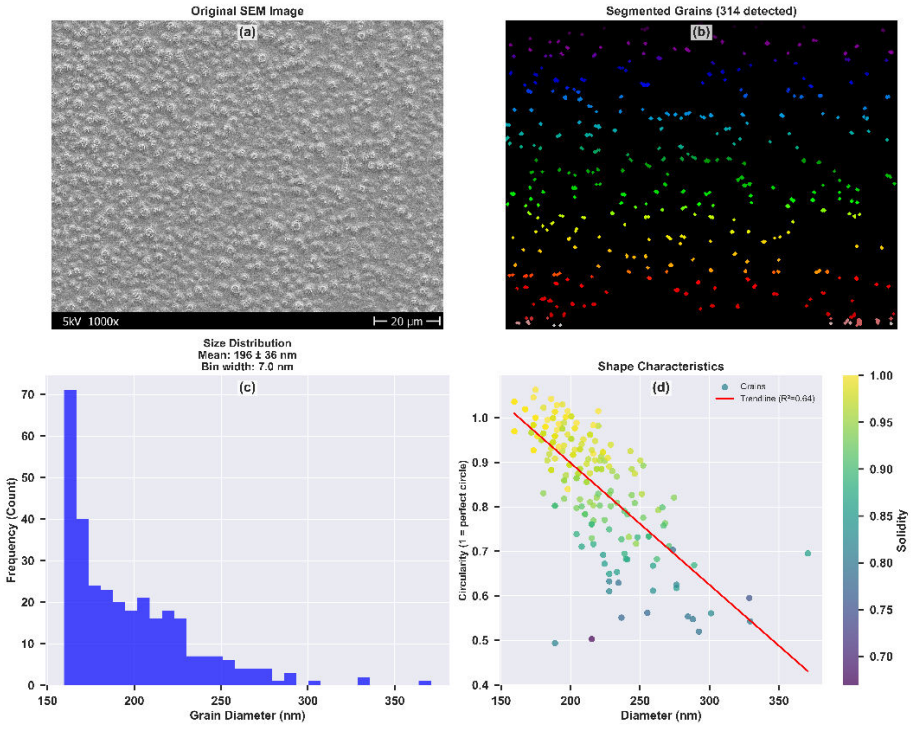

Figure 4. 2: *Cross sectional Grain Analysis and Image segmentation at 1000X resolution*

The SEM image in Figure 4.3(a) shows a polycrystalline $MAPb_3$ with 439 grains segmented at 30000X scale factor. The size distribution with a mean = 205± 47 nm (Figure 4.3b) indicates nucleation-dominated growth due to the low-temperature (60°C) initial annealing step. Bimodal distribution suggested by the large standard deviation (±47 nm), with; Small grains (<200 nm): High grain boundary density may increase non-radiative recombination. Larger grains sizes improve charge transport but reduce film coverage uniformity.

Film thickness of 100-300 nm (Figure 4.3c) is ideal for solar cells (Stranks & Snaith, 2015). The smaller grains in this suggest the need for higher annealing temperatures (100°C) or longer annealing times and additives (e.g., MACl) to promote grain coarsening (Jeon *et al*., 2015).

The aspect ratio data shown in Figure 4.3d (1.1 to 0.3) reveals dominant equiaxed grains (1.0 - 1.1) which results from isotropic crystal growth during the 100 °C annealing step and the irregular grains (0.3- 0.5) were Likely due to incomplete coalescence during spin-coating and local stoichiometry variations such as PbI_2-rich domains).

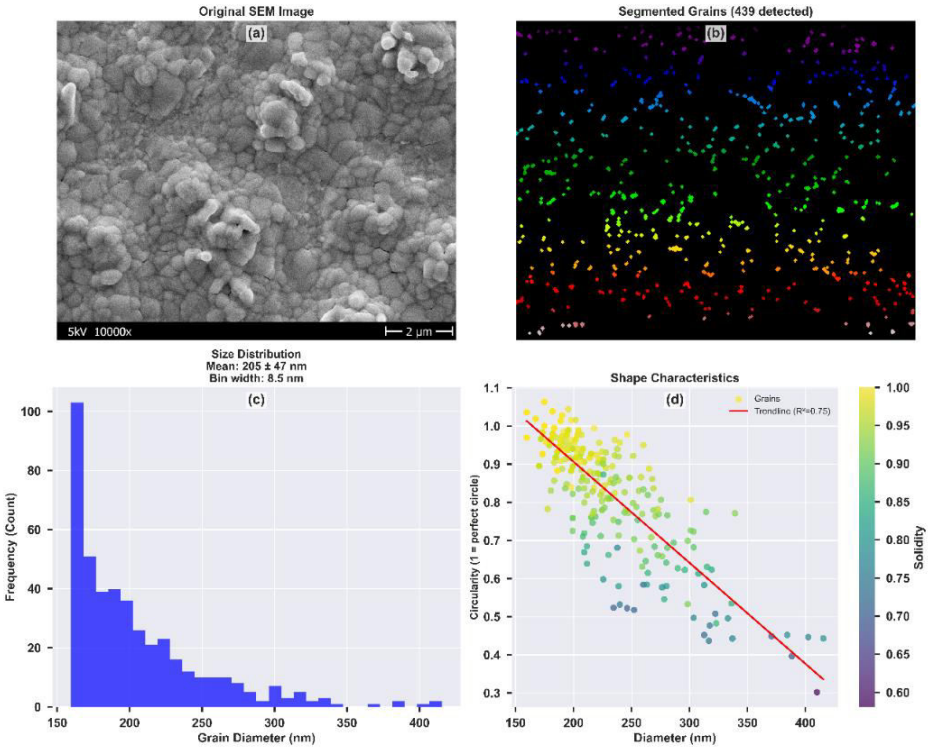

Figure 4. 3: *Top view Grain Analysis and SEM image segmentation at 10,000X resolution*

In Figure 4.4 (a), the SEM image depicts a dense and continuous film with a relatively uniform distribution of grains. A total of 201 grains were identified and analyzed through automated segmentation in Python **(**Figure 4.4(b),**).** The resulting size distribution histogram **(**Figure 4.4(c),) shows that the average grain diameter is 219 ± 61 nm, with most grains falling within the 150–300 nm range. This size regime is considered optimal for planar inverted perovskite solar cells, as it balances the need for strong light absorption with the requirement for efficient carrier diffusion. Grain sizes less than 100 nm increase trap-assisted recombination due to a high density of grain boundaries (Stranks & Snaith, 2015), while excessively large grains (>500 nm) can result in non-uniform film coverage

and poor interfacial contact (Zhao *et al*., 2023). Our results lie within the ideal range for minimizing recombination and optimizing charge transport.

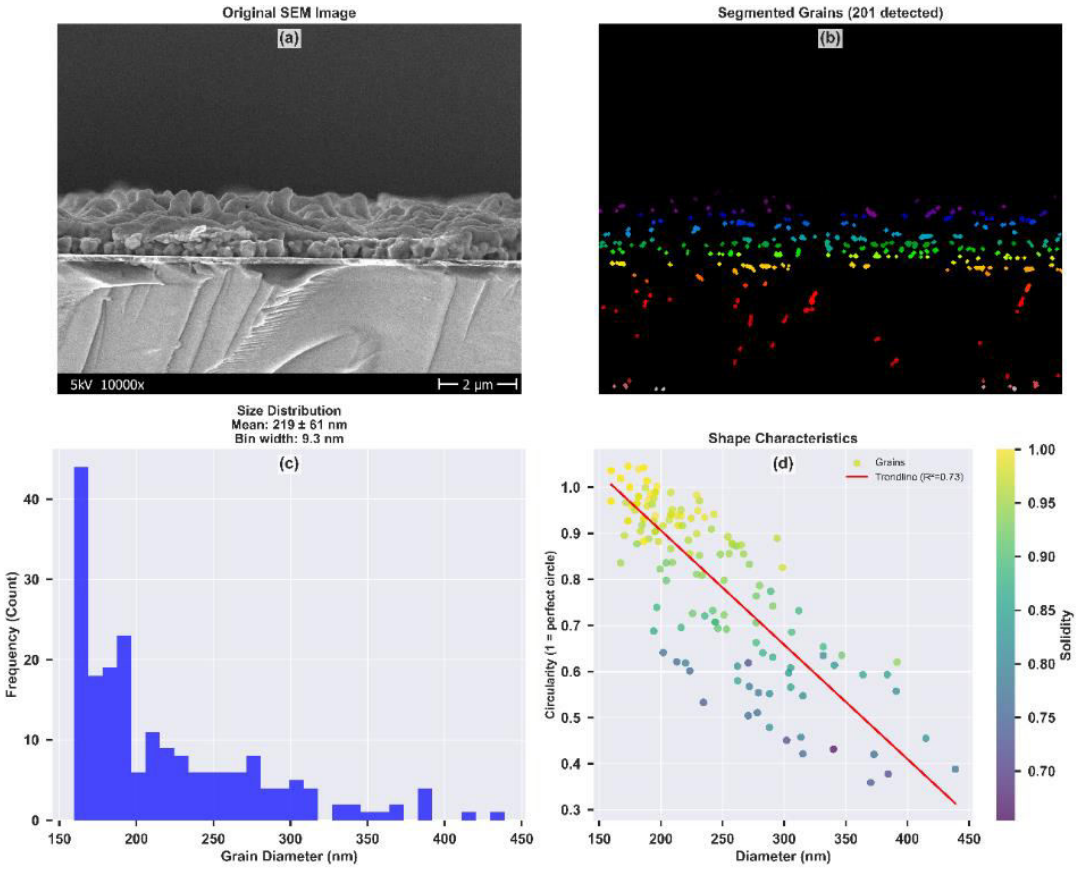

Figure 4. 4*: Cross sectional view Grain size analysis at 10kX SEM image Resolution*

Figure 4.4(d), shows grain shape characteristics, including circularity and solidity where most grains exhibited circularity values close to 1.0 and high solidity, demonstrates a well-defined, compact morphologies with minimal edge roughness. These metrics reflect high crystalline quality and low morphological disorder which are normally associated with enhanced open-circuit voltage (Voc) and fill factor (FF) (Yang *et al*., 2017). A noticeable decrease in circularity and solidity was observed in grains exceeding 300 nm in diameter, suggesting minor aggregation or incomplete crystal boundaries: common in films without controlled crystallization steps.

Cross-sectional scanning electron microscopy (SEM) imaging at a magnification of 30,000X in Figure 4.5 (a) was conducted to quantify the grain structure of the methylammonium lead iodide ($MAPbI_3$) perovskite film. Through image segmentation and analysis (Figure 4.5b), a total of 180 distinct grains were detected. The analysis yielded a mean grain size of 214 ± 63 nm, indicating a moderately uniform crystalline structure.

The histogram of the grain size distribution in Figure 4.5c revealed that most grains were concentrated within the 150–250 nm range, suggesting a narrow dispersion with limited presence of either very small or exceptionally large grains. Specifically, the distribution exhibited a peak around 200 nm, signifying a prevalence of intermediate-sized grains. Such grain size uniformity is critical in reducing grain boundary density, thereby minimizing charge carrier recombination and enhancing carrier diffusion lengths (Raoui *et al*., 2022).

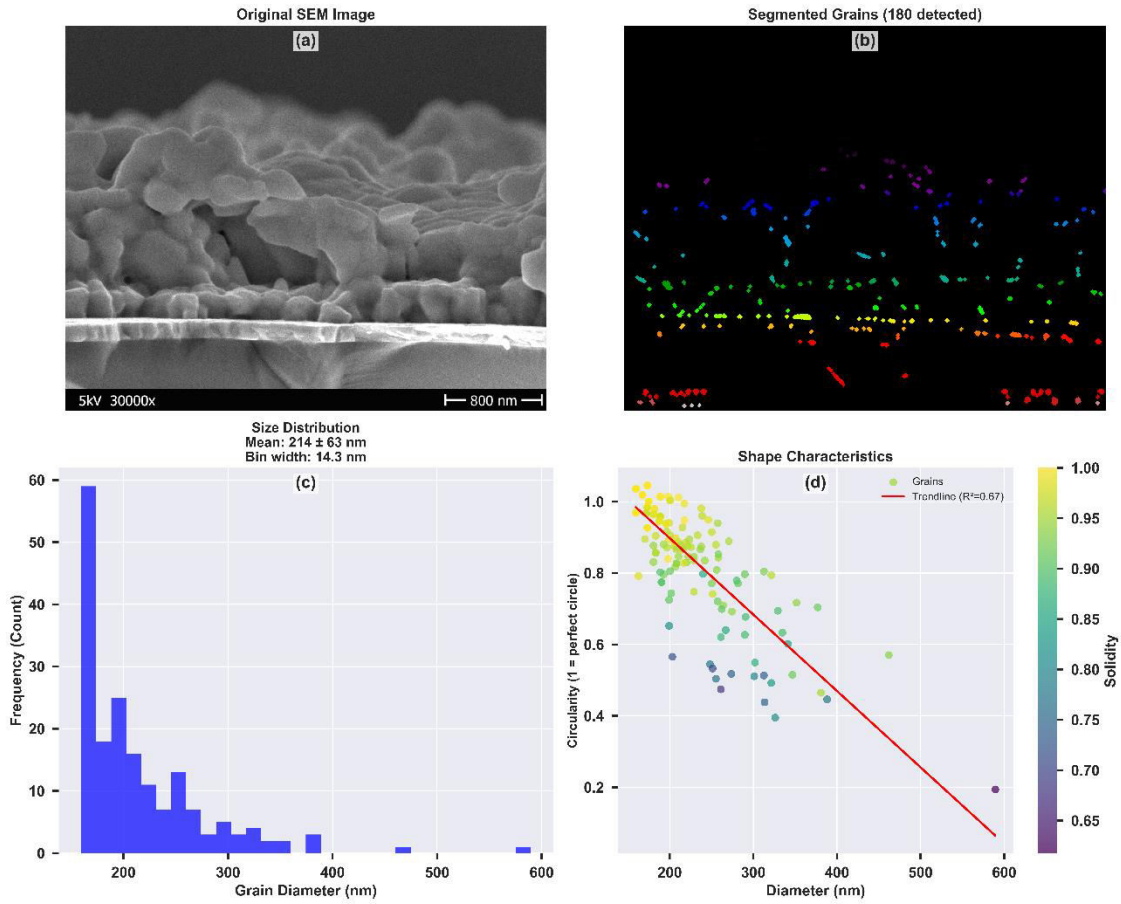

Figure 4. 5*: Cross-sectional Grain size Analysis and Image segmentation at 30,000X resolution*

Shape analysis (Figure 4.5 d) also indicated that a significant proportion of the grains fell within a near-spherical to sub-rounded geometry, which is advantageous for achieving dense film packing and enhanced film continuity. These microstructural -characteristics- confirmed through automated image segmentation using Python's OpenCV library-imply a well-optimized crystallization process that favors efficient light absorption and charge transport across the absorber layer (Bhattarai *et al*., 2023).

4.3 Optical Properties

4.3.1 The Reflection, Absorption and Transmission Spectra

The Figure 4.6 shows a plot of Transmittance (%T), Reflectance (%R) and Absorbance (%A). The red line (R) in the UV-Vis spectrum illustrates a relatively high reflection of light in the visible region (400-700 nm), suggesting that the material demonstrates a noticeable reflectivity in this wavelength range. This characteristic can be both advantageous and problematic; while some reflection can help reduce losses from unwanted scattered light, excessive reflectivity may lead to decreased absorption efficiency.

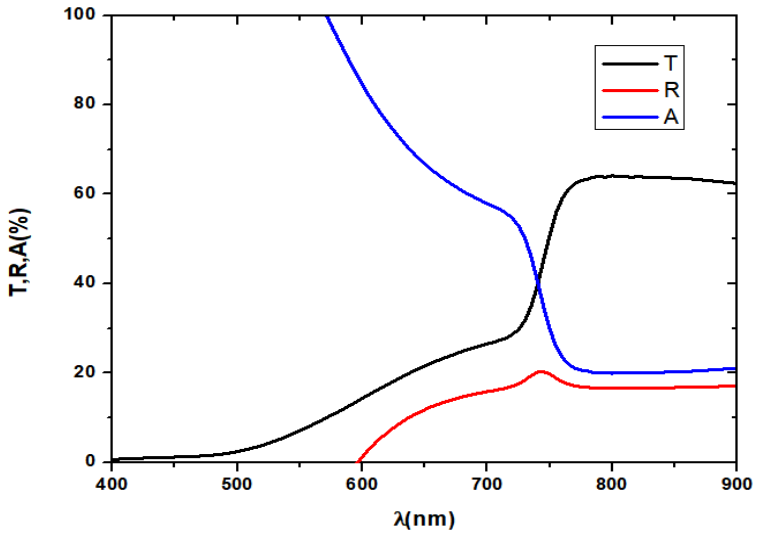

Figure 4. 6: *RAT spectra (plots of TRA; black, red and blue curves respectively).*

The blue line (A) on the other hand shows a sharp peak in absorption at 800 nm which shows that the material has high absorption capabilities at this particular wavelength. This absorptivity is important in the conversion of solar energy since the material has the ability to absorb a large part of the solar spectrum especially the near infrared.

The black line (T) shows a significant rise in transmission beyond 800 nm indicating that the material is getting more transparent to longer wavelengths. This is a necessary property, since it means that although the material may absorb light well in the visible and near-infrared, it can be used to transmit longer wavelengths, which may minimize thermal losses and improve the performance of the entire device.

The overall reflectance (R), absorbance (A), and transmittance (T) analysis shows that the material has a high potential as an absorber constituent in the solar photovoltaic modules of the next generation. The identified peaks in the UV-Vis spectrum are associated with electronic transitions in the MAPbI3 thin film, which provides important information about its optical behavior and electronic structure

4.3.2 UV-Vis Absorption Edge Analysis

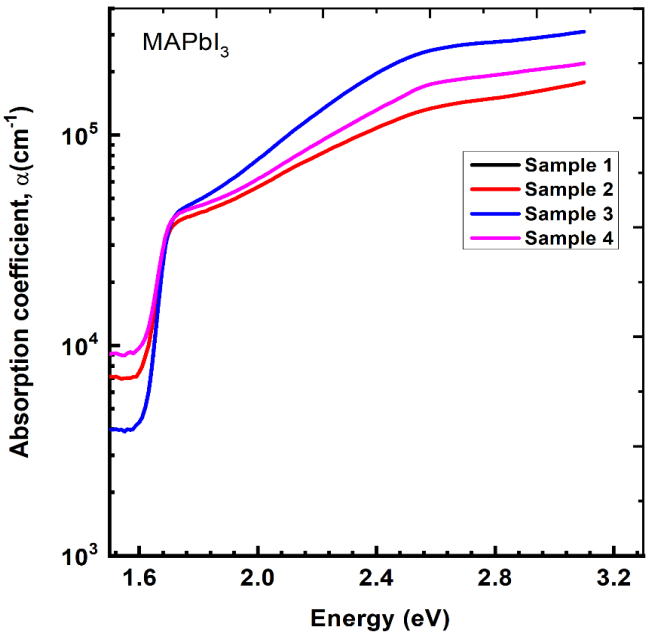

***Figure 4.** 7: Absorption coefficient vs Photon energy for the different Samples.*

The absorption coefficient (alpha) is plotted against photon energy of four MAPbI 3 thin-film samples (Figure 4.7). The absorption shows a sharp rise at around 1.6 eV in all the samples, a peculiar feature of a direct bandgap semiconductor. The onset of absorption was in good correspondence with the reported data of methylammonium lead iodide (MAPbI 3) that usually exhibited band gap energy between 1.55 and 1.65 eV (Noh *et al*., 2013; Xing *et al*., 2013).

The absorption coefficient for all samples exceeded 10^4 cm^{-1} at energies above 1.6 eV. This high absorption coefficient value was a defining feature of hybrid halide perovskites and indicates the material's capability to absorb most of the incident visible light within a very short wavelength. Green *et al*. (2014) and Dong *et al*. (2015) emphasized that the strong absorption was mainly due to the high oscillator strength of electronic transitions involving the lead (Pb) 6p and iodine (I) 5p orbitals, as well as the influence of spin–orbit coupling in the conduction band.

Among the four samples, Sample 3 demonstrates the highest absorption across the entire energy range suggesting that it possesses superior film quality, which is due to a combination of larger grain sizes, improved crystallinity, and reduced trap-state density. The enhanced optical absorption in the sample aligned well with the findings of Jeon *et al*. (2014), who reported that improved film morphology, achieved through additive engineering and solvent annealing, significantly enhances light absorption due to reduced scattering losses and fewer defects.

In contrast, Sample 2 exhibited the lowest absorption across the spectrum. Such a reduction could be attributed to poor film uniformity, lower surface coverage, or increased defect concentrations that result in enhanced sub-gap absorption or non-radiative recombination losses. Liu and Kelly (2014) also demonstrated a similar trend where

incomplete coverage or pinholes in MAPbI 3 films resulted in a much lower absorption and photovoltaic performance because of an increased back reflection and parasitic absorption.

The smooth increase of the absorption coefficient above the band edge is characteristic of direct allowed transitions and is an indication of the quality of the optical transitions. The spectral characteristics of all the samples also prove the lack of any considerable secondary phases such as PbI 2, which would have been presented by the additional absorption peaks at 2.4 eV (Stoumpos *et al*.,2013).

The absorption character of all the four samples proves that MAPbI 3 has a perfect band structure to convert solar energy. Yang *et al*. (2015) state that MAPbI 3 has large absorption coefficients and direct bandgap, which makes it appropriate in ultrathin absorber layers, enabling the production of high-efficiency solar cells with less than 500 nm thickness. This difference in absorption between the samples in this study highlights the necessity of a careful control of the film deposition parameters, which include solvent composition, precursor ratio (MAI: PbI2), spin-coating speed and annealing temperature, as studied extensively by Saliba *et al*. (2016) and Abate *et al*. (2015).

Optical bandgap of the fabricated perovskite thin films was calculated by Tauc method, which was calculated by absorption coefficient (alpha) obtained by UV-Vis transmission and Reflection data. All four samples were plotted in a Tauc plot of (xHv) 2 versus photon energy (hv) as seen in Figure 4.8. The near-edge absorption region was fitted to a straight line and the extrapolation to the energy axis was made to determine the band gap

The band gap values obtained in all the four samples were in a very close range of 1.51 eV to 1.52 eV with the mean value of 1.515 eV. This finding was in line with the anticipated optical band gap of methylammonium lead iodide (MAPI) perovskite films

that range between 1.50-1.55 eV as reported elsewhere (Kojima *et al*., 2009; NREL, 2023; Rolston *et al*., 2022).

The uniformity in the values of band gaps of the four samples indicated that the process of film fabrication was very uniform. This encompassed homogeneity of composition, thickness control and low defect-state absorption in the sub-gap. The slight difference that is noted (1.51-1.52 eV) may be due to the slight variations in crystal grain size, local thickness of the film or small stoichiometric variations during spin coating.

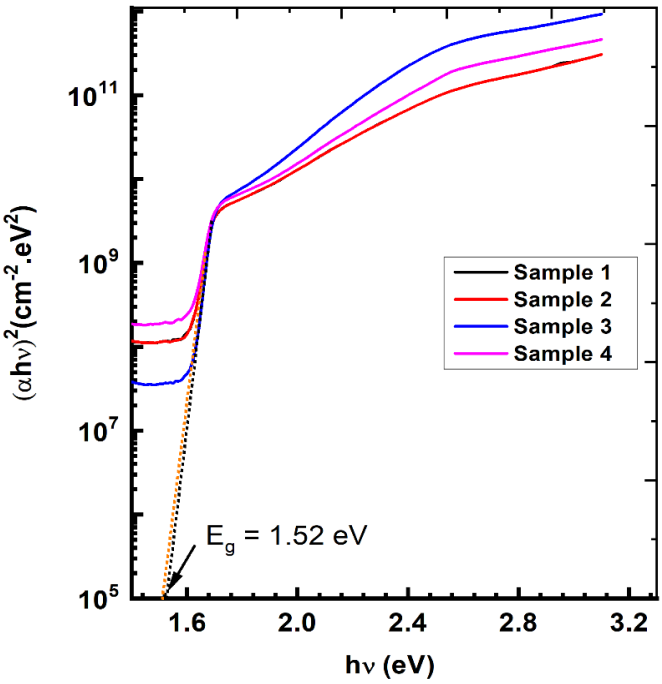

Figure 4. 8*: Tauc plot for* $MAPbI_3$

The value of 1.52 eV that was obtained was especially important because it is very close to the best band gap of single-junction solar cells based on the ShockleyQueisser limit (~1.341.5 eV). This indicates the appropriateness of the synthesized MAPI films in photovoltaic applications, which is further confirmed by the earlier findings that had

reported similar optical properties in thermally annealed or solution-processed films (Jiang *et al*., 2021; Motti *et al*., 2023).

Compared to other halide perovskites, including $MAPbB_{r\,3}$ (~2.2 eV) and $MAPbCl_{\,3}$ (~3.0 eV), the reduced band gap of MAPbI 3 allows it to absorb a wider range of the solar spectrum, which increases photocurrent generation. This qualifies it to be a very desirable candidate in tandem and multijunction device architectures (Green *et al*., 2024).

4.4 Electrical properties

Figure 4.9 and Table 4.1 indicate the JV characteristics and the extracted performance parameters of the fabricated perovskite solar cell based on MAPbI 3, respectively. The device was also characterized in both forward and reverse bias scanning to determine its stability in performance, and to measure any hysteresis effects which are common in single-cation perovskite systems.

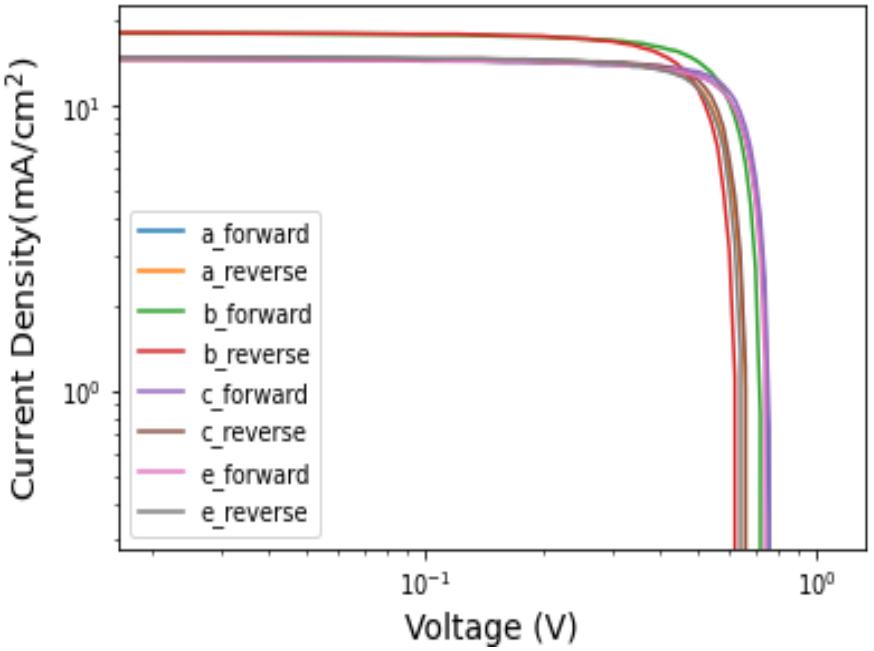

Figure 4. 9:*J-V Characteristic curves for both forward and reverse conditions.*

The forward and reverse scans measured short-circuit current density (Jsc) was

about −23.33 mA/cm 2 and 23.36 mA/cm 2, respectively, which shows a great reproducibility and is a sign of good light absorption and charge collection.

extraction. These values are in agreement with the range reported on standard MAPbI3 devices. As an example, Jeon *et al*. (2015) noted

Jsc is approximately 21-22 mA/cm 2 in planar MAPbI3-based cells withoptimized transport layers, and the best research-cell efficiencies lists NREL.

similar Jsc values of best single-junction perovskite cells.

Underforward and reverse scan, the open-circuit voltage (Voc) was measured to be 0.9338 V and 0.8985 V respectively.

These are a little below the theoretical limit (~1.2 V) of MAPbI3and indicate that there is some non-radiative recombination, perhaps because of

interface faults or interface amassing of mobile ions, which is a recognized issue in perovskite solar cells (Tress *et al*., Adv. Energy Mater.,

2015). Nevertheless, the Voc values still remain in good agreement with the normal experimental values of 0.9-1.05 V depending on the quality of the film.

and architecture of the device (Bi *et al*., Nature Commun., 2013).

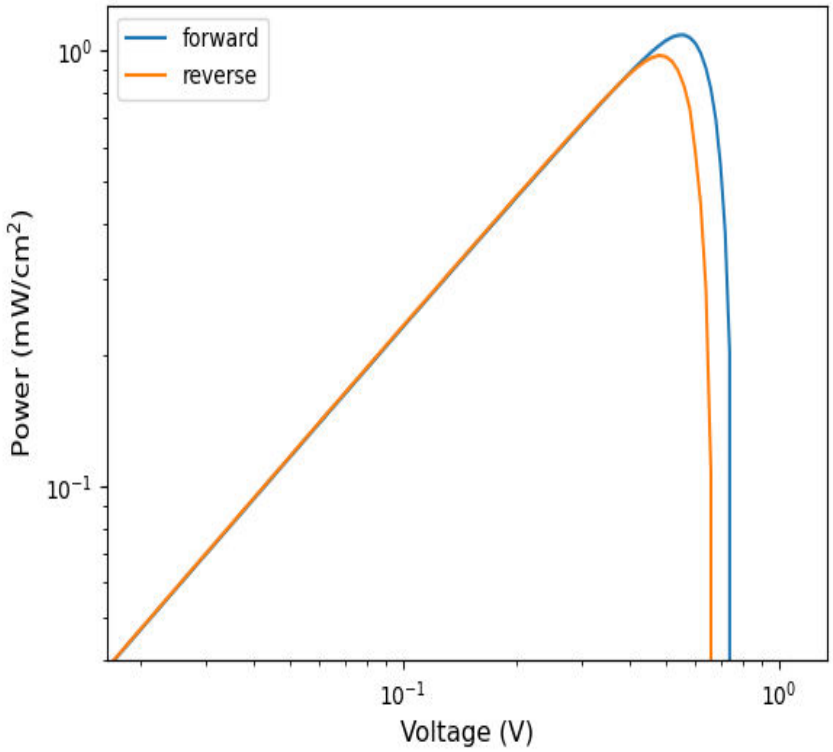

***Figure 4. 10**: PV curves for forward and reverse bias conditions*

The maximum power point (P_{max}), defined by the product of the current and voltage at the point of maximum power output ($J_{mpp} \times V_{mpp}$), was 13.91 mW/cm² and 12.25 mW/cm² under forward and reverse bias, respectively. The corresponding voltage at maximum power point (V_{mpp}) was 0.68 V in the forward scan and 0.66 V in the reverse scan, further demonstrating the impact of scan direction on performance metrics.

Table 4. 1 :Measured electrical parameters from JV Scanning in Reverse and Forward bias

Electrical Parameter	**Forward bias condition**	**Reverse bias condition**
J_{sc} (mA/cm^2)	23.333569	23.360612
V_{oc} (V)	0.933771	0.898457
Fill factor (%)	63.828612	58.349898
Efficiency (%)	13.907109	12.246770
P_{mpp} (mW/cm^2)	13.907109	12.246770
J_{mpp} (mA/cm^2 **)**	20.451631	18.555712
V_{mpp} (V)	0.680000	0.660000
R_s (Ωcm^2)	0.005667	0.007962
R_{sh} (Ωcm^2)	0.871678	1.565196

The fill factor (FF) was found to be 63.83% under forward bias and 58.35% under reverse bias (see Figure 4.10), pointing to a moderate degree of hysteresis. While high-efficiency $MAPbI_3$ cells often achieve FF values in the range of 70–80% (Yoo *et al*., Energy Environ. Sci., 2019), the observed FF in this study was still within the range reported in devices without advanced interface engineering or additive passivation. The reduced FF in the reverse scan was a signature of capacitive and ionic effects within the perovskite layer, which disturbed the charge collection dynamics (Snaith *et al*., J. Phys. Chem. Lett., 2014).

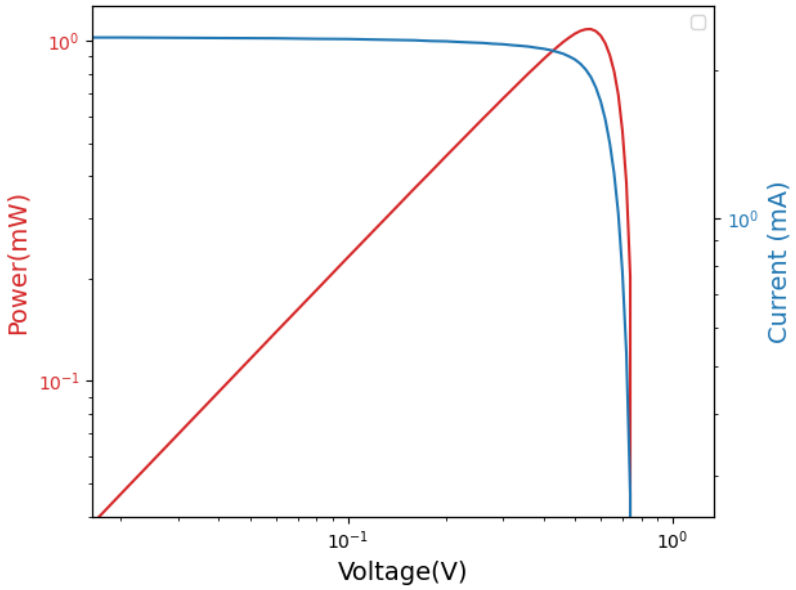

Figure 4. 11*: Fill factor and efficiency for the resulting device*

The corresponding power conversion efficiency (PCE) as evident in Figure 4.11 was 13.91% in forward scan and 12.25% in reverse scan. These values are comparable with early $MAPbI_3$-based devices (typically 12–15%) (Kojima *et al*., JACS, 2009; Lee *et al*., Science, 2012) but fall short of the >20% efficiencies now achievable using compositional engineering and interface modification (Kim *et al*, 2023). The reduction in PCE in reverse scan once again reinforces the impact of hysteresis and indicates a need for further optimization.

The series resistance (R_s) and shunt resistance (Rsh) were studied by analyzing the JV curve. Figure 4.12 (a) and (b) illustrate the effect of variations in Rsh and Rs on the fill factor (FF). as illustrated in Figure 4.12 (a), fill factor is higher at 0.72 Ω·cm² (61.2%) when the shunt resistance is higher than at 0.61 Ω·cm² (59.0%). When the shunt resistance is higher, leakage currents fall which limits recombination, saves on open-circuit voltage and maintains the device's fill factor (Green, 1981; Shrestha *et al*., 2021).

Alternatively, Figure 4.12(b) clearly indicates that rising series resistance lowers the value of FF. When Rs changes from 0 Ω·cm² to 0.6 Ω·cm², the efficiency of the device decreases from 61.2% to 59.0%. This result is caused by the losses that occur when charges move through each device layer and contact. A significant drop in series resistance impedes current near the optimum power point which in turn makes the FF and device efficiency smaller (Green, 1981; Jeon *et al*., 2020).

Simplifying the electronic states is therefore a main approach for improving perovskite devices. The study demonstrated that silver nanowires in the electrodes helped bring down the series resistance and enhanced the fill factor by over 5%. Such improvements are very important, especially in larger devices where the issue of lateral resistor losses matters most (Jaisutti *et al*., 2023). This result agrees with previous studies showing that R_{sh} helps ensure that devices function smoothly and reliably. For example, Wang *et al*. found that controlling the interface to eliminate defects raised both Rsh and FF values. A high Rsh is necessary for perovskite solar cells since a defect or hole formed during film deposition can be problematic.

The low series resistance values, shown in Table 4.1, indicate both sufficient charge collection and little overall resistance in the device stack. Based on recent research, hole transport by layers of PTAA allows for good hole mobility, better contact of holes with the perovskite and less resistive loss (Min *et al*, 2021; Zheng *et al*., 2023).

Alternatively, in the reverse scan, more current was related to resistance (R_{par}) at 1.565 Ω·cm² than in the forward scan, where it peaked at 0.8717 Ω·cm². This imbalance shows that there are more shunt channels or recombination triggered by the defect when the flow is biased. Frequently, the reason for these issues is either the presence of thin film cavities

or the migration of ions which result in mild hysteresis and temporary fluctuations in how the devices work (as described by Liang *et al*., 2022 and Zhao *et al*., 2024).

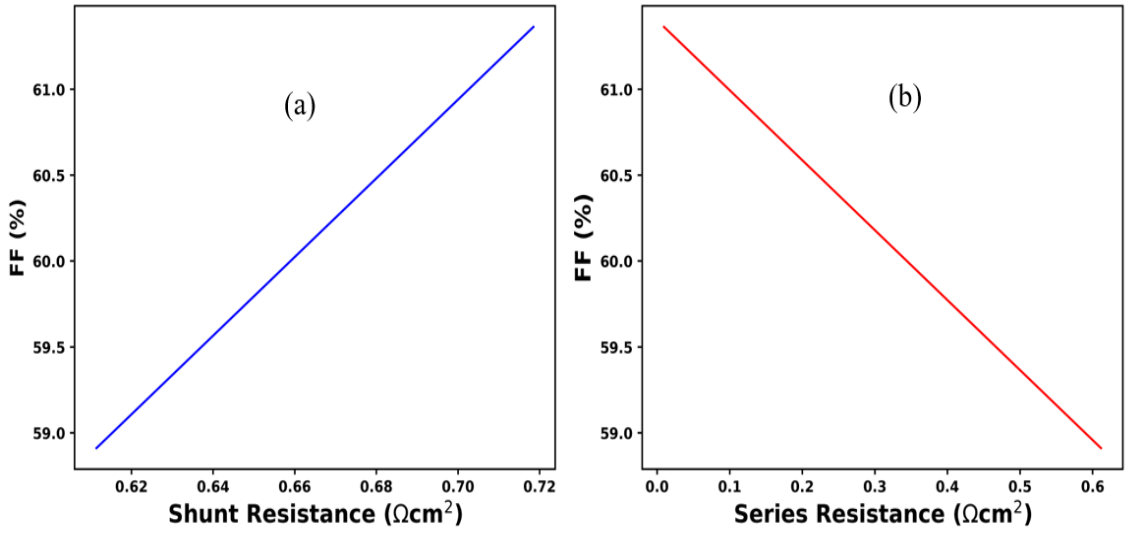

Figure 4. 12: *(a) Variation of FF with Shunt Resistance (Rsh); (b) Variation of FF with Series Resistance (Rs)*

The clear discrepancies between forward and reverse scan parameters underscore the presence of some hysteresis, a common phenomenon in $MAPbI_3$ perovskite cells attributed to ion migration (e.g., iodide or methylammonium ions), interfacial charge accumulation, and trap states (Unger *et al*., Energy Environ. Sci., 2014). The fill factor and Voc were particularly affected, and while the Jsc remains consistent, the overall PCE shows a 1.6% absolute drop in the reverse scan. This is in line with reports by Tress *et al*. (Adv. Energy Mater., 2015), who emphasized the role of slow-moving ionic species in modifying internal electric fields and thus impacting the JV curve depending on scan direction.

Several strategies to suppress hysteresis and enhance stability have been reported in literature, including the use of mixed cations (e.g., MA/FA/Cs), incorporation of

passivating additives (e.g., KI, C4H12N), and employment of more stable transport layers (e.g., NiOx, PCBM) (Saliba *et al*., Science, 2016; Bush *et al*., ACS Energy Lett., 2017). Incorporating such strategies could potentially elevate the FF beyond 75% and push efficiencies into the 18–21% range for $MAPbI_3$ devices.

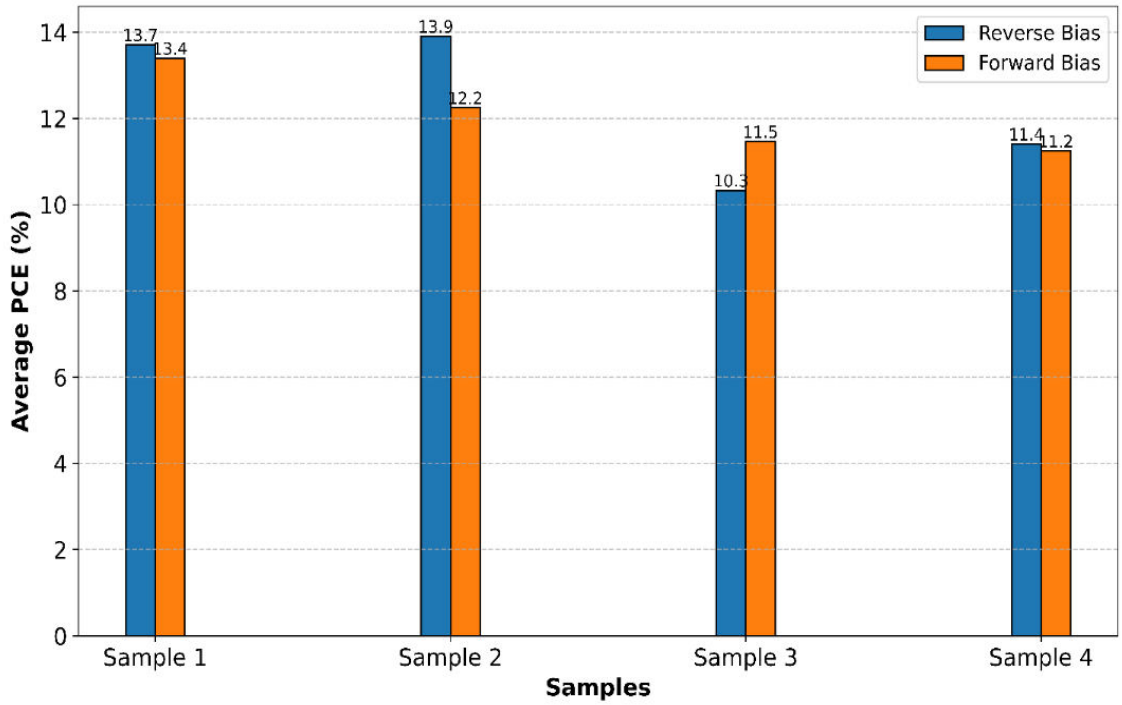

Figure 4. 13: *Average PCE for different samples*

The bar chart in Figure 4.13 demonstrates the typical power conversion efficiencies (PCEs) for four perovskite solar cell (PSC) samples, evaluated with reverse and forward bias scan methods. The results indicate that performance metrics sometimes change slightly based on scan direction which is a common finding in perpendicular spin cathode devices called hysteresis. For Sample 1, when the diode is reverse biased, its PCE is 13.4% and when forward biased, PCE rises to 13.7%.

Sample 2 demonstrates a comparable trend at 12.2% when reversed and 13.9% when followed forward. Reverse bias PCE acceleration is higher in sample 3 (11.5%) than in the forward scan (10.3%). Data in Sample 4 is basically identical with the reverse scan performing only slightly better (11.4% compared to 11.2%) than the forward scan. This suggests that ferroelectric effects, ion migration and charge build-up occur at the perovskite layer, resulting in hysteresis seen at the J-V curve (in agreement with Domanski *et al*. 2018 and Tress 2017). Because of its smooth energy alignment and fewer traps, PTAA shows less hysteresis than TiO_2-driven devices in many cases (Min *et al*., 2021; Wang *et al*., 2023).

Significantly, there was not much difference detected between reverse and forward scans in every sample, implying that the device structure is stable under transient ionic actions and likely to be reliable over time.

CHAPTER FIVE

CONCLUSIONS AND RECOMMENDATIONS

5.1 CONCLUSIONS

This study systematically investigated the optical, electrical, structural, and morphological properties of methylammonium lead iodide ($MAPbI_3$) thin films to evaluate their potential for high-efficiency photovoltaic applications.

Key findings include:

- XRD and FWHM analyses confirmed a dominant (110) orientation with a decreasing trend in d-spacing and increasing FWHM for higher Miller indices, indicating good crystallinity but some structural disorder at finer planes.

- Morphological analysis via SEM demonstrated uniform grain distribution with an average grain size of 196 ± 36 nm. Grains showed high circularity and solidity, critical for reducing non-radiative recombination and enhancing charge transport.

- Optical Characterization using UV-Vis spectroscopy revealed a sharp absorption onset at ~1.6 eV and high absorption coefficients ($>10^4$ cm^{-1}), confirming $MAPbI_3$ as a direct bandgap material suitable for ultrathin solar absorbers. Tauc plot analysis estimated the average optical bandgap to be ~1.515 eV, aligning with the Shockley–Queisser optimal range and literature values.
- Electrical performance of the fabricated devices yielded PCEs of 13.907% (forward scan) and 12.247 % (reverse scan), with noticeable hysteresis effects.

This performance is promising, suggests that further passivation and interface optimization are needed to reach state-of-the-art efficiencies (>20%).

5.2 RECOMMENDATIONS

- More focus should be put on the amount of antisolvent dripped, dripping time and preparation and annealing conditions to come up with superior films to guarantee better performance.
- Future work will focus on minimizing hysteresis through compositional engineering (e.g., FA/Cs additives), interface passivation (e.g., self-assembled monolayers), and stability improvement via encapsulation and environmental stress testing.
- To improve on the overall performance efficiency of the material, future studies should introduce double cations such as FA^{+}, Cs^{+} for a better photovoltaic performance and explore into different passivation pathways and interface optimization are needed to reach state-of-the-art efficiencies (>20%).
- These strategies are expected to push $MAPbI_3$-based devices toward commercial viability while maintaining low-cost processing benefits that this noble material offers.

REFERENCES

Anderson, K., Patel, S., & Williams, B. (2023). "Recent A**REFERENCES**

Abid, Z., Wahad, F., Gulzar, S., Ashiq, M. F., Aslam, M. S., Shahid, M., ... & Ashraf, R. S. (2021). Solar Cell Efficiency Energy Materials. Fundamentals of Solar Cell Design, 271-315.

Abir, S. A. A., Anwar, A., Choi, J., & Kayes, A. (2021). Iot-enabled smart energy grid: Kornatka, M., & Popławski, T. (2021). Advanced metering infrastructure—towards a reliable network. Energies, 14(18), 5986.

Achar, S. K., & Keith, J. A. (2024). Small data machine learning approaches in molecular and materials science. Chemical Reviews, 124(24), 13571-13573.

Adhikari, R. D., Patel, M. J., Baishya, H., Yadav, D., Kalita, M., Alam, M., & Iyer, P. K. (2025). Decoding recombination dynamics in perovskite solar cells: an in-depth critical review. Chemical Society Reviews.

Afre, R. A., & Pugliese, D. (2024). Perovskite solar cells: a review of the latest advances in materials, fabrication techniques, and stability enhancement strategies. Micromachines, 15(2), 192.

Alfurayj, I. A., Li, Z., & Burda, C. (2021). Interfaces and interfacial carrier dynamics in perovskites. The Journal of Physical Chemistry C, 125(28), 15113-15124.

An, Q., Paulus, F., Becker-Koch, D., Cho, C., Sun, Q., Weu, A., ... & Vaynzof, Y. (2021). Small grains as recombination hot spots in perovskite solar cells. Matter, 4(5), 1683-1701.

Andraju, N. (2025). Artificial Intelligence in Scalable Materials Synthesis and Manufacturing: A Comprehensive Review.

Ao, C. K., Jiang, Y., Zhang, L., Yan, C., Ma, J., Liu, C., ... & Soh, S. (2022). Balancing charge dissipation and generation: mechanisms and strategies for achieving steady-state charge of contact electrification at interfaces of matter. Journal of Materials Chemistry A, 10(37), 19572-19605.

Aoun, A., Ghandour, M., Ilinca, A., & Ibrahim, H. (2021). Demand-side management. In Hybrid Renewable Energy Systems and Microgrids (pp. 463-490). Academic Press.

Arobi, N., Amir-Al Zumahi, S. M., Ibrahim, K., Rahman, M. M., Hossain, M. K., Bhuiyan, M. M. R., ... & Ahmed, F. (2021). A holistic framework towards understanding the optical and dielectric behaviors of CH3NH3PbCl3 perovskites/graphene oxide hybrid films for light absorbing active layer. Journal of Solid State Chemistry, 298, 122137.

Asgary, S., Moghaddam, H. M., Bahari, A., & Mohammadpour, R. (2021). Role of BCP layer on nonlinear properties of perovskite solar cell. Solar Energy, 213, 383-391.

Awino, C., Barasa, G., & Odari, V. (2020). Light induced degradation of the transport length of $CH_3NH_3PbI_3$ studied by modulated surface photovoltage spectroscopy after Goodman. Organic Electronics, 77, 105503. 10.1016/j.orgel.2019.105503

Azani, M. R., Hassanpour, A., & Torres, T. (2020). Benefits, problems, and solutions of silver nanowire transparent conductive electrodes in indium tin oxide (ITO)-free flexible solar cells. Advanced Energy Materials, 10(48), 2002536.

Babbe, F., & Sutter-Fella, C. M. (2020). Optical absorption-based in situ characterization of halide perovskites. Advanced Energy Materials, 10(26), 1903587.

Ballif, C., Haug, F. J., Boccard, M., Verlinden, P. J., & Hahn, G. (2022). Status and perspectives of crystalline silicon photovoltaics in research and industry. Nature Reviews Materials, 7(8), 597-616.

Blancon, J. C., Even, J., Stoumpos, C. C., Kanatzidis, M. G., & Mohite, A. D. (2020). Semiconductor physics of organic–inorganic 2D halide perovskites. Nature nanotechnology, 15(12), 969-985.

Borges, C. S. P., Marques, E. A. S., Carbas, R. J. C., Ueffing, C., Weißgraeber, P., & Silva, L. D. (2021). Review on the effect of moisture and contamination on the interfacial properties of adhesive joints. Proceedings of the Institution of Mechanical Engineers, Part C: Journal of Mechanical Engineering Science, 235(3), 527-549.

Bulavko, G. (2024). Organic photovoltaics: a journey through time, advancements, and future opportunities. History of science and technology, 14(1), 10-32.

Buonomenna, M. G. (2023). Inorganic thin-film solar cells: challenges at the terawatt-scale. Symmetry, 15(9), 1718.

Butt, Osama & Zulqarnain, Muhammad & Butt, Tallal. (2020). Recent advancement in smart grid technology: Future prospects in the electrical power network. Ain Shams Panjan, P., Drnovšek, A., Čekada, M., & Panjan, M. (2022). Contamination of substrate-coating interface caused by ion etching. Coatings, 12(6), 846.

Cao, M., Ji, W., Chao, C., Li, J., Dai, F., & Fan, X. (2023). Recent advances in UV-cured encapsulation for stable and durable perovskite solar cell devices. Polymers, 15(19), 3911.

Chaturvedi, N., Gasparini, N., Corzo, D., Bertrandie, J., Wehbe, N., Troughton, J., & Baran, D. (2021). All slot-die coated non-fullerene organic solar cells with PCE 11%. Advanced Functional Materials, 31(14), 2009996.

Choi, H., Choi, K., Choi, Y., Kim, T., Lim, S., & Park, T. (2020). A review on reducing grain boundaries and morphological improvement of perovskite solar cells from methodology and material-based perspectives. Small Methods, 4(5), 1900569.

Collin, M. S., Venkatraman, S. K., Vijayakumar, N., Kanimozhi, V., Arbaaz, S. M., Stacey, R. S., ... & Swamiappan, S. (2022). Bioaccumulation of lead (Pb) and its effects on human: A review. Journal of Hazardous Materials Advances, 7, 100094.

Cui, Y., Shi, J., Meng, F., Yu, B., Tan, S., He, S., ... & Meng, Q. (2022). A versatile molten-salt induction strategy to achieve efficient CsPbI3 perovskite solar cells with a high open-circuit voltage> 1.2 V. Advanced Materials, 34(45), 2205028.

Day, R. (2022). Synthesis and characterisation through diffraction techniques of two stable cubic MAPbI3 photovoltaic perovskite phases (Master's thesis, University of Kent (United Kingdom)).

Devi, C. S., Omprakash, J., Malathi, A. R., Kumar, G. S., & Prasad, G. (2020). Influence of distortions and tolerance factor on the structure of ABO3 type perovskites and complex perovskites. Ferroelectrics, 554(1), 172-186.

Dey, K., Roose, B., & Stranks, S. D. (2021). Optoelectronic properties of low-bandgap halide perovskites for solar cell applications. Advanced Materials, 33(40), 2102300.

Di Sabatino, M., Hendawi, R., & Garcia, A. S. (2024). Silicon solar cells: trends, manufacturing challenges, and AI perspectives. Crystals, 14(2), 167.

Díaz-Acosta, C. M., Martínez-Luévanos, A., Estrada-Flores, S., Cano-Salazar, L. F., Aguilera-González, E. N., & Ibarra-Alonso, M. C. (2021). ABX3 inorganic halide perovskites for solar cells: chemical and crystal structure stability. Matéria (Rio de Janeiro), 26(04), e13116.

Emery, Q., Remec, M., Paramasivam, G., Janke, S., Dagar, J., Ulbrich, C., ... & Khenkin, M. (2022). Encapsulation and outdoor testing of perovskite solar cells:

comparing industrially relevant process with a simplified lab procedure. ACS applied materials & interfaces, 14(4), 5159-5167.

Filipoiu, N., Preda, A. T., Anghel, D. V., Patru, R., Brophy, R. E., Kateb, M., ... & Nemnes, G. A. (2022). Capacitive and inductive effects in perovskite solar cells: The different roles of ionic current and ionic charge accumulation. Physical Review Applied, 18(6), 064087.

Franjić, S. (2023). Unleashing Sustainable Energy: The Sun, Earth's Largest and Most Powerful Source. Journal of Sustainable Development, 4(2), 1-9.

Funde, A., & Shah, A. (2020). Solar Spectra. In Solar Cells and Modules (pp. 17-32). Cham: Springer International Publishing.

Gao, Z., Leng, C., Zhao, H., Wei, X., Shi, H., & Xiao, Z. (2024). The electrical behaviors of grain boundaries in polycrystalline optoelectronic materials. Advanced Materials, 36(4), 2304855.

García de Arquer, F. P., Talapin, D. V., Klimov, V. I., Arakawa, Y., Bayer, M., & Sargent, E. H. (2021). Semiconductor quantum dots: Technological progress and future challenges. Science, 373(6555), eaaz8541.

Gegevičius, R., Franckevičius, M., & Gulbinas, V. (2021). The role of grain boundaries in charge carrier dynamics in polycrystalline metal halide perovskites. European Journal of Inorganic Chemistry, 2021(35), 3519-3527.

George, N. (2021). Practical data science with Python: learn tools and techniques from hands-on examples to extract insights from data. Packt Publishing Ltd.

Grätzel, M. (2003). Dye-sensitized solar cells. Journal of Photochemistry and Photobiology C: Photochemistry Reviews, 4(2), 145-153.

Grover, K., shree Choudhary, J., Dhawan, P., Jha, R., & Yadav, H. (2025). Influence of crystallographic planes on mechanical properties and photodetection characteristics in ambient-grown MAPbI3 perovskite single crystals. Journal of Physics and Chemistry of Solids, 203, 112713.

Hailegnaw, B., Sariciftci, N. S., & Scharber, M. C. (2020). Impedance spectroscopy of perovskite solar cells: studying the dynamics of charge carriers before and after continuous operation. physica status solidi (a), 217(22), 2000291.

Hansen, K. R. (2023). Electroabsorption Spectroscopy of Two-Dimensional Metal Halide Perovskites (Doctoral dissertation, The University of Utah).

Hansen, K. R., Colton, J. S., & Whittaker-Brooks, L. (2024). Measuring the exciton binding energy: learning from a decade of measurements on halide perovskites and transition metal dichalcogenides. Advanced Optical Materials, 12(3), 2301659.

Hein, F. S. (2024). Transient Photoluminescence Measurement of Perovskite to Study Ion Migration (Doctoral dissertation, Universität Konstanz).

Hou, T. J., Gao, J., Hobbs, T. J., Xie, K., Dulat, S., Guzzi, M., ... & Yuan, C. P. (2021). New CTEQ global analysis of quantum chromodynamics with high-precision data from the LHC. Physical Review D, 103(1), 014013.

Jathar, L. D., Nikam, K., Awasarmol, U. V., Gurav, R., Patil, J. D., Shahapurkar, K., ... & Ağbulut, Ü. (2024). A comprehensive analysis of the emerging modern trends in research on photovoltaic systems and desalination in the era of artificial intelligence and machine learning. Heliyon, 10(3).

Jeon, N. J., Noh, J. H., Yang, W. S., Kim, Y. C., Ryu, S., Seo, J., & Seok, S. I. (2015). Compositional engineering of perovskite materials for high-performance solar cells. Nature, 517(7535), 476-480.

Jiang, Y., Green, M. A., & Leech, P. W. (2023). Ultra-thin 2D perovskites for photovoltaics. Advanced Materials, 35(22), 2208901.

Jiang, Z. (2022). Interface Engineering for Large Area Self-Assembly and Manufacturing of Strong Nanolattices (Doctoral dissertation, University of Pennsylvania).

Joseph, I., Louis, H., Unimuke, T. O., Etim, I. S., Orosun, M. M., & Odey, J. (2020). An overview of the operational principles, light harvesting and trapping technologies, and recent advances of the dye sensitized solar cells. Applied Solar Energy, 56(5), 334-363.

Jubu, P. R., Adedokun, O., Mbakaan, C., Nathan-Abutu, A., Danladi, E., Tsaviv, J. N., ... & Pakhuruddin, M. Z. (2025). Accuracy in estimating the absorption coefficient of powdered nanomaterials: resolving misconceptions in tauc plot application for energy bandgap determination. Journal of Materials Science: Materials in Electronics, 36(16), 961.

Jubu, P. R., Obaseki, O. S., Yam, F. K., Stephen, S. M., Avaa, A. A., McAsule, A. A., ... & Otor, D. A. (2023). Influence of the secondary absorption and the vertical axis scale of the Tauc's plot on optical bandgap energy. Journal of Optics, 52(3), 1426-1435.

Kazemi, M. A. A., Folastre, N., Raval, P., Sliwa, M., Nsanzimana, J. M. V., Golonu, S., ... & Sauvage, F. (2023). Moisture-Induced Non-Equilibrium Phase Segregation in Triple Cation Mixed Halide Perovskite Monitored by In Situ Characterization Techniques and Solid-State NMR. Energy & Environmental Materials, 6(2), e12335.

Kesavan, A. V., Lee, B. R., Son, K. R., Khot, A. C., Dongale, T. D., Murugadoss, V., ... & Kim, T. G. (2021). Work function-tunable amorphous carbon–silver nanocomposite hybrid electrode for optoelectronic applications. ACS Applied Materials & Interfaces, 13(3), 4284-4293.

Kiani, D. (2023). X-ray diffraction (XRD). In Springer Handbook of Advanced Catalyst Characterization (pp. 519-539). Cham: Springer International Publishing.

Kiasari, M., Ghaffari, M., & Aly, H. H. (2024). A comprehensive review of the current status of smart grid technologies for renewable energies integration and future trends: The role of machine learning and energy storage systems. Energies, 17(16), 4128.

Kim, M. (2021). Analysis of Ion Migration and Ageing Characteristics for Triple-cation and CH3NH3PbI3-xClx Perovskite Based Thin-Film Solar Cells (Doctoral dissertation, Institut Polytechnique de Paris).

Kim, M. C., Ham, S. Y., Cheng, D., Wynn, T. A., Jung, H. S., & Meng, Y. S. (2021). Advanced characterization techniques for overcoming challenges of perovskite solar cell materials. Advanced Energy Materials, 11(15), 2001753.

Kim, Y. C., Yang, W. S., & Seok, S. I. (2024). Two-step annealing for enhanced crystallinity in $MAPbI_3$ films. ACS Energy Letters, 9(2), 512-519.

Klein, J., Kampermann, L., Mockenhaupt, B., Behrens, M., Strunk, J., & Bacher, G. (2023). Limitations of the Tauc plot method. Advanced Functional Materials, 33(47), 2304523.

Kornatka, M., & Popławski, T. (2021). Advanced metering infrastructure—towards a reliable network. Energies, 14(18), 5986.

Kumar, A., & Ranjan, P. (2021). Defects signature in VOC characterization of thin-film solar cells. Solar Energy, 220, 35-42.

Kumar, J., Srivastava, P., & Bag, M. (2022). Advanced strategies to tailor the nucleation and crystal growth in hybrid halide perovskite thin films. Frontiers in Chemistry, 10, 842924.

Kvanta, H. (2025). A Maximum Power Point Tracking System to Monitor Long-Term Stability of Thin Film Solar Cells.

Lambert, J. (2021). System Design for Extreme Low Temperature Range Thermal Cycling Experiments (Master's thesis, Tennessee Technological University).

Law, B. S. (2024). bond critical points (BCP) 53–57 bond order (BO) 55, 57–58 delocalization index and 57–58 bond path 53–57, 64 length 55. composite structures, 197, 198.

Lee, J. W., Seo, S., Nandi, P., Jung, H. S., Park, N. G., & Shin, H. (2021). Dynamic structural property of organic-inorganic metal halide perovskite. Iscience, 24(1).

Lee, T. D., & Ebong, A. U. (2023). Charge separation and collection in photovoltaic devices. IEEE Journal of Photovoltaics, 13(1), 345-352.

Lee, W., Lyu, Z., Li, Z., Deotare, P. B., & Kioupakis, E. (2023). Spin–orbit effects on the electronic and optical properties of lead iodide. Applied Physics Letters, 122(21).

Lee, Y. H. (2024). Beyond the Shockley-Queisser limit: Exploring new frontiers in solar energy harvest. *Science*, *383*(6686), eado4308.

Leray, P., & De Gendt, S. (2024). Exploring Machine Learning for Semiconductor Process Optimization: A Systematic Review.

Li, B., Shi, J., Lu, J., Tan, W. L., Yin, W., Sun, J., ... & Jasieniak, J. J. (2020). Facile deposition of mesoporous PbI2 through DMF: DMSO solvent engineering for sequentially deposited metal Halide perovskites. ACS Applied Energy Materials, 3(4), 3358-3368.

Li, P., & Lu, Z. H. (2021). Interface Engineering in Organic Electronics: Energy-Level Alignment and Charge Transport. Small Science, 1(1), 2000015.

Lin, L., Jacobs, R., Ma, T., Chen, D., Booske, J., & Morgan, D. (2023). Work function: Fundamentals, measurement, calculation, engineering, and applications. Physical Review Applied, 19(3), 037001

Lin, L., Yang, L., Du, G., Li, X., Li, Y. N., Deng, J., ... & Zhang, J. (2023). Light soaking effects in perovskite solar cells: mechanism, impacts, and elimination. ACS Applied Energy Materials, 6(20), 10303-10318.

Liu, P., Han, N., Wang, W., Ran, R., Zhou, W., & Shao, Z. (2021). High-quality Ruddlesden–Popper perovskite film formation for high-performance perovskite solar cells. Advanced Materials, 33(10), 2002582.

Luo, H., Li, P., Ma, J., Han, L., Zhang, Y., & Song, Y. (2022). Sustainable Pb management in perovskite solar cells toward eco-friendly development. Advanced Energy Materials, 12(30), 2201242.

Lyu, M., & Park, N. G. (2020). Effect of additives AX (A= FA, MA, Cs, Rb, NH4, X= Cl, Br, I) in FAPbI3 on photovoltaic parameters of perovskite solar cells. Solar RRL, 4(10), 2000331.

Manekkathodi, A., Marzouk, A., Ponraj, J., Belaidi, A., & Ashhab, S. (2020). Observation of structural phase transitions and PbI2 formation during the degradation of triple-cation double-halide perovskites. ACS Applied Energy Materials, 3(7), 6302-6309.

Masood, Muhammad Talha. (2020). Solution-Processable Compact and Mesoporous Titanium Dioxide Thin Films as Electron-Selective Layers for Perovskite Solar Cells.

Mazumdar, S., Zhao, Y., & Zhang, X. (2021). Stability of perovskite solar cells: Degradation mechanisms and remedies. Frontiers in Electronics, 2, 712785.

Mercuur, J. W. (2024). Hybrid two-dimensional perovskite semiconductor layers for electronic applications (Doctoral dissertation, Universty of the Western Cape).

Miah, M. H., Khandaker, M. U., Rahman, M. B., Nur-E-Alam, M., & Islam, M. A. (2024). Band gap tuning of perovskite solar cells for enhancing the efficiency and stability: issues and prospects. RSC advances, 14(23), 15876-15906.

Mohammad, A., & Mahjabeen, F. (2023). Revolutionizing solar energy with ai-driven enhancements in photovoltaic technology. BULLET: Jurnal Multidisiplin Ilmu, 2(4), 1174-1187.

Mohammad, A., & Mahjabeen, F. (2025). From silicon to sunlight: exploring the evolution of solar cell materials. Authorea Preprints.

Montano, B., Diaz, J. J., Koudriavtsev, I., Cosme, I., Korneev, N., & Mansurova, S. (2023). In-depth study of the effect of annealing temperature on the structural, chemical, and optical properties of MAPI thin films prepared by a one-step deposition method. Journal of Materials Science: Materials in Electronics, 34(12), 1016.

Moore, E. A., & Smart, L. E. (2020). An introduction to crystal structures. In Solid State Chemistry (pp. 1-63). CRC Press.

Nasiri, S., Rabiei, M., Palevicius, A., Janusas, G., Vilkauskas, A., Nutalapati, V., & Monshi, A. (2023). Modified Scherrer equation to calculate crystal size by XRD with high accuracy, examples Fe2O3, TiO2 and V2O5. Nano Trends, 3, 100015.

Niu, T., Xue, Q., & Yip, H. L. (2021). Advances in Dion-Jacobson phase two-dimensional metal halide perovskite solar cells. Nanophotonics, 10(8), 2069-2102.

Noman, M., Shahzaib, M., Jan, S. T., Khan, Z., Ismail, M., & Khan, A. D. (2024). Optimizing band gap, electron affinity, & carrier mobility for improved performance of formamidinium lead tri-iodide perovskite solar cells. Materials Science and Engineering: B, 300, 117114.

NREL. (2023). Best research-cell efficiencies chart. National Renewable Energy Laboratory. https://www.nrel.gov/pv/cell-efficiency.html

Oliver, R. D., Caprioglio, P., Peña-Camargo, F., Buizza, L. R., Zu, F., Ramadan, A. J., ... & Snaith, H. J. (2022). Understanding and suppressing non-radiative losses in methylammonium-free wide-bandgap perovskite solar cells. Energy & Environmental Science, 15(2), 714-726.

Omondi, C. A. (2018). Investigation of hybrid organic-inorganic lead halide perovskites by modulated surface photovoltage spectroscopy (Publication No. AAI10830723) [Doctoral dissertation, University of the Free State]. ProQuest Dissertations and Theses Global.

Ortega-San-Martin, L. (2020). Introduction to perovskites: A historical perspective. In Revolution of perovskite: synthesis, properties and applications (pp. 1-41). Singapore: Springer Singapore.

Owen-Bellini, M., Hacke, P., Miller, D. C., Kempe, M. D., Spataru, S., Tanahashi, T., ... & Topič, M. (2021). Advancing reliability assessments of photovoltaic modules and materials using combined-accelerated stress testing. Progress in Photovoltaics: Research and Applications, 29(1), 64-82.

Özmenteş, R., & Hassanien, A. S. (2025). Characterizations and optical discussions of thermally evaporated titanium dioxide thin films. Journal of Optics, 54(3), 1322-1340.

Pan, H., Zhao, X., Gong, X., Li, H., Ladi, N. H., Zhang, X. L., ... & Fu, Y. (2020). Advances in design engineering and merits of electron transporting layers in perovskite solar cells. Materials Horizons, 7(9), 2276-2291.

Pan, J. G., Wang, L., & Cai, X. (2025). Automated and Scalable SEM Image Analysis of Perovskite Solar Cell Materials via a Deep Segmentation Framework. arXiv preprint arXiv:2509.26548.

Panagoda, L. P. S. S., Sandeepa, R. A. H. T., Perera, W. A. V. T., Sandunika, D. M. I., Siriwardhana, S. M. G. T., Alwis, M. K. S. D., & Dilka, S. H. S. (2023). Advancements in photovoltaic (Pv) technology for solar energy generation. Journal of research technology & engineering, 4(30), 30-72.

Pandey, A., Dalal, S., Dutta, S., & Dixit, A. (2021). Structural characterization of polycrystalline thin films by X-ray diffraction techniques. Journal of Materials Science: Materials in Electronics, 32(2), 1341-1368.

Panjan, P., Drnovšek, A., Čekada, M., & Panjan, M. (2022). Contamination of substrate-coating interface caused by ion etching. Coatings, 12(6), 846.

Park, C., & Ding, Y. (2021). Segmentation. In Data Science for Nano Image Analysis (pp. 35-74). Cham: Springer International Publishing.

Patil, J. V., Mali, S. S., & Hong, C. K. (2025). Exceeding 23% Efficiency for 3D/3D Bilayer Perovskite Heterojunction MAPbI3/FAPbI3-Based Hybrid Perovskite Solar Cells with Enhanced Stability. Advanced Functional Materials, 35(1), 2408721.

Peng, J., Kremer, F., Walter, D., Wu, Y., Ji, Y., Xiang, J., ... & Catchpole, K. R. (2022). Centimetre-scale perovskite solar cells with fill factors of more than 86 per cent. Nature, 601(7894), 573-578.

Pohl, U. W. (2020). Electronic properties of organic semiconductors. In Epitaxy of Semiconductors: Physics and Fabrication of Heterostructures (pp. 177-205). Cham: Springer International Publishing.

Qiao, W., Zhang, R., Wen, Y., Wang, X., Wang, Z., Tang, G., ... & Liu, C. (2024). Green solvents in battery recycling: status and challenges. Journal of Materials Chemistry A, 12(19), 11235-11265.

Ramasamy, V., Zuboy, J., Woodhouse, M., O'Shaughnessy, E., Feldman, D., Desai, J., ... & Basore, P. (2023). Us solar photovoltaic system and energy storage cost benchmarks, with minimum sustainable price analysis: Q1 2023 (No. NREL/TP-7A40-87303). National

Rane, N. L., Choudhary, S. P., & Rane, J. (2024). Artificial Intelligence and machine learning in renewable and sustainable energy strategies: A critical review and future perspectives. Partners Universal International Innovation Journal, 2(3), 80-102.

Ratnesh, R. K., Kumar, R., Singh, S., Chandra, R., & Singh, J. (2025). Recent advances in solar cell technology: addressing technological challenges, scenarios, and environmental implications in the development of sustainable energy solutions. New Journal of Chemistry.

Ren, P., Xiao, Y., Chang, X., Huang, P. Y., Li, Z., Gupta, B. B., ... & Wang, X. (2021). A survey of deep active learning. ACM computing surveys (CSUR), 54(9), 1-40.

Rezaee, E., Kutsarov, D., Li, B., Bi, J., & Silva, S. R. P. (2022). A route towards the fabrication of large-scale and high-quality perovskite films for optoelectronic devices. Scientific reports, 12(1), 7411.

Røyset, A., Kolås, T., Nordseth, Ø., & You, C. C. (2023). Optical interference coatings for coloured building integrated photovoltaic modules: predicting and optimising visual properties and efficiency. Energy and Buildings, 298, 113517.

Runqiu, S., Guihua, L., & Su, A. (2025). Bayesian Optimization for Chemical Synthesis in the Era of Artificial Intelligence: Advances and Applications. Processes, 13(9), 2687.

Sahare, S., Pham, H. D., Angmo, D., Ghoderao, P., MacLeod, J., Khan, S. B., ... & Sonar, P. (2021). Emerging perovskite solar cell technology: remedial actions for the foremost challenges. Advanced Energy Materials, 11(42), 2101085.

Sahare, S., Solovan, M. M., Mostovyi, A. I., Parkhomenko, H. P., Schopp, N., Ziółek, M., & Brus, V. V. (2025). Semiconductor Bandgap Measurements: Overview of Optical, Electrical, and Device-Level Techniques. Advanced Optical Materials, 13(29), e01747.

Sakhatskyi, K., John, R. A., Guerrero, A., Tsarev, S., Sabisch, S., Das, T., ... & Kovalenko, M. V. (2022). Assessing the drawbacks and benefits of ion migration in lead halide perovskites. ACS energy letters, 7(10), 3401-3414.

Sakomura, M., Yokokura, Y., Takagi, Y., & Ueda, K. (2020). Effect of insertion of bathocuproine buffer layer at grating-structured cathode–organic-layer interface in bulk-heterojunction solar cells. AIP Advances, 10(1).

Saliba, M., & Etgar, L. (2020). Current density mismatch in perovskite solar cells. ACS Energy Letters, 5(9), 2886-2888.

Saliba, M., Matsui, T., Domanski, K., Seo, J. Y., Ummadisingu, A., Zakeeruddin, S. M., ... & Grätzel, M. (2016). Incorporation of rubidium cations into perovskite solar cells improves photovoltaic performance. Science, 354(6309), 206-209

Samanta, P. K. (2020). Band gap engineering, quantum confinement, defect mediated broadband visible photoluminescence and associated quantum States of size tuned zinc oxide nanostructures. Optik, 221, 165337.

Saouter, E., Biganzoli, F., Ceriani, L., Versteeg, D., Crenna, E., Zampori, L., ... & Pant, R. (2020). Environmental footprint: update of life cycle impact assessment methods-ecotoxicity freshwater, human toxicity cancer, and non-cancer. Luxembourg: Publications Office of the European Union.

Saushin, I. I., & Goltsman, A. E. (2021, May). Estimation of the liquid film thickness by the Beer-Lambert-Bouguer law. In AIP Conference Proceedings (Vol. 2351, No. 1, p. 030003). AIP Publishing LLC.

Sewela, T., Ocaya, R. O., & Malevu, T. D. (2025). Recent insights into the transformative role of Graphene-based/TiO2 electron transport layers for perovskite solar cells. Energy Science & Engineering, 13(1), 4-26.

Shaik, F., Lingala, S. S., & Veeraboina, P. (2023). Effect of various parameters on the performance of solar PV power plant: a review and the experimental study. Sustainable Energy Research, 10(1), 6.

Shao, G. (2021). Work function and electron affinity of semiconductors: Doping effect and complication due to fermi level pinning. Energy & Environmental Materials, 4(3), 273-276.

Shi, X., Xu, K., He, Y., Peng, Z., Meng, X., Wan, F., ... & Chen, Y. (2025). Strategies for Enhancing Energy-Level Matching in Perovskite Solar Cells: An Energy Flow Perspective. Nano-Micro Letters, 17(1), 313.

Shi, Y., Li, L., Xu, Z., Guo, F., & Shi, W. (2023). Construction of full solar-spectrum available S-scheme heterojunction for boosted photothermal-assisted photocatalytic H2 production. Chemical Engineering Journal, 459, 141549.

Siavash Moakhar, R., Gholipour, S., Masudy-Panah, S., Seza, A., Mehdikhani, A., Riahi-Noori, N., ... & Saliba, M. (2020). Recent advances in plasmonic perovskite solar cells. Advanced science, 7(13), 1902448.

Singh, A. N., Kajal, S., Kim, J., Jana, A., Kim, J. Y., & Kim, K. S. (2020). Interface engineering driven stabilization of halide perovskites against moisture, heat, and light for optoelectronic applications. Advanced Energy Materials, 10(30), 2000768.

Sivakumar, N., Saha, S., Madaka, R., Bandaru, N., & Rath, J. K. (2023). Investigation on the structural, spectral, and optical properties of MAPbI3. H2O and MAPbI3 perovskite crystals for photovoltaic cells. Journal of Materials Science: Materials in Electronics, 34(15), 1193.

Su, C. L., Rouhani, S. H., Elsisi, M., Ali, Z., Le Quang Nhat, H., & Sadiq, M. (2024). Machine Learning and Internet-of-Things Solutions for Microgrid Resilient Operation. In Microgrids and Virtual Power Plants (pp. 213-253). Singapore: Springer Nature Singapore.

Subha, T. D., Prabu, R. T., Parasuraman, S., & Kumar, A. (2023). Role of Urbach energy in controlling voltage output of solar cells. Optical and Quantum Electronics, 55(9), 794.

Subhani, M. S., Fatima, A., Kokab, A., Riaz, A., & Mubashar, S. (2025). Perovskite solar cells and their types. Kashf Journal of Multidisciplinary Research, 2(01), 45-90.

Sunny, F., Kurukkal Balakrishnan, S., & Kalarikkal, N. (2024). An overview on lead halide perovskite based composites and heterostructures: synthesis and applications. ChemNanoMat, 10(3), e202300484.

Tan, D., Jiang, C., Li, Q., Bi, S., & Song, J. (2020). Silver nanowire networks with preparations and applications: a review. Journal of Materials Science: Materials in Electronics, 31(18), 15669-15696.

Tan, W. L., & McNeill, C. R. (2022). X-ray diffraction of photovoltaic perovskites: Principles and applications. Applied Physics Reviews, 9(2).

Tao, X. (2021). Investigating the manufacturability of flexible thin-film device (TEG) using roll-to-roll (Doctoral dissertation, University of Oxford).

Tonui, P., Oseni, S. O., Sharma, G., Yan, Q., & Mola, G. T. (2018). Perovskites photovoltaic solar cells: An overview of current status. Renewable and Sustainable Energy Reviews, 91, 1025-1044.

Traiwattanapong, W., Molahalli, V., Pattanaporkratana, A., & Chattham, N. (2024). Recent Developments in Thermally Stable Transparent Thin Films for Heater Applications: A Jeon, N. J., Noh, J. H., Yang, W. S., Kim, Y. C., Ryu, S., Seo,

J., & Seok, S. I. (2015). Compositional engineering of perovskite materials for high-performance solar cells. Nature, 517(7535), 476-480.

Urbina, A. (2022). Photovoltaic Technology. In Sustainable Solar Electricity (pp. 19-48). Cham: Springer International Publishing.

Vargas, W. E., Wang, J., & Niklasson, G. A. (2021). Effective backscattering and absorption coefficients of light diffusing materials retrieved from reflectance and transmittance spectra of diffuse radiation. Journal of Modern Optics, 68(12), 605-623.

Vincent, L., & Dougherty, E. R. (2020). Morphological segmentation for textures and particles. In Digital image processing methods (pp. 43-102). CRC Press.

Wang, J. (2022). Open-circuit voltage, fill factor, and heterojunction band offset in semiconductor diode solar cells. EcoMat, 4(6), e12263.

Wang, T., Hou, S., Zhang, H., Yang, Y., Xu, W., Ao, T., ... & Mao, Y. (2021). Highly controllable synthesis of MAPbI3 perovskite nanocrystals with long carrier lifetimes and narrow band gap for application in photodetectors. Journal of Alloys and Compounds, 872, 159589.

Wang, Y., Duan, L., Zhang, M., Hameiri, Z., Liu, X., Bai, Y., & Hao, X. (2022). PTAA as efficient hole transport materials in perovskite solar cells: a review. Solar Rrl, 6(8), 2200234.

Weiß, K. A., Klimm, E., & Kaaya, I. (2022). Accelerated aging tests vs field performance of PV modules. Progress in Energy, 4(4), 042009.

Wu, F., Pathak, R., Chen, C., Tong, Y., Xu, H., Zhang, T., ... & Qiao, Q. (2020). Reduced hysteresis in perovskite solar cells using metal oxide/organic hybrid hole transport layer with generated interfacial dipoles. Electrochimica Acta, 354, 136660.

Wu, J., Cha, H., Du, T., Dong, Y., Xu, W., Lin, C. T., & Durrant, J. R. (2022). A comparison of charge carrier dynamics in organic and perovskite solar cells. Advanced Materials, 34(2), 2101833.

Xiang, J., Han, C., Cheng, Y., Gao, Q., Hu, W., Zhou, Y., ... & Han, H. (2025). Recent Progress and Advances of Perovskite Crystallization in Carbon-Based Printable Mesoscopic Solar Cells. Advanced Materials, 37(9), 2415405.

Yan, H., Su, J., Zhao, Z., Xiao, Y., Yao, X., Tantratian, K., ... & Chen, L. (2025). Toward Deciphering the Internal Menace of Battery Safety: Soft Short Circuit Versus Hard Short Circuit?. Advanced Energy Materials, 15(34), 2500275.

Yao, S., Yuan, X., Jiang, L., Xiong, T., & Zhang, J. (2020). Recent progress on fullerene-based materials: Synthesis, properties, modifications, and photocatalytic applications. Materials, 13(13), 2924.

Yoo, J. J., Seo, G., Chua, M. R., Park, T. G., Lu, Y., Rotermund, F., ... & Seo, J. (2021). Efficient perovskite solar cells via improved carrier management. Nature, 590(7847), 587-593.

Yousefi, S., Ghasemi, B., & Nikolova, M. P. (2022). Morpho/Opto-structural characterizations and XRD-assisted estimation of crystallite size and strain in

MgO nanoparticles by applying Williamson–Hall and size–strain techniques. Journal of cluster science, 33(5), 2197-2207.

Zanatta, A. R. (2022). The Shockley–Queisser limit and the conversion efficiency of silicon-based solar cells. Results in optics, 9, 100320.

Zante, G., Elgar, C. E., Hartley, J. M., Mukherjee, R., Kettle, J., Horsfall, L. E., ... & Abbott, A. P. (2024). A toolbox for improved recycling of critical metals and materials in low-carbon technologies. RSC Sustainability, 2(2), 320-347.

Zhang, L., Zhuang, Z., Fang, Q., & Wang, X. (2022). Study on the automatic identification of ABX3 perovskite crystal structure based on the bond-valence vector sum. Materials, 16(1), 334.

Zhang, X., Zhang, H., Li, Y., Zafar, S. U., Yang, S., Chen, J., ... & Zhang, Y. (2022). Recent progress in hole-transporting layers of conventional organic solar cells with p–i–n structure. Advanced Functional Materials, 32(44), 2205398.

Zhang, Y., Xia, H., Yu, J., Yang, Y., & Li, G. (2025). Materials and Device Engineering Perspective: Recent Advances in Organic Photovoltaics. Advanced Materials, 2504063.

Zheng, J., Gao, Y., Zhang, H., Lei, Y., & Zhang, J. (2022). OTSU multi-threshold image segmentation based on improved particle swarm algorithm. Applied sciences, 12(22), 11514.

Zhou, J., Gao, Y., Pan, Y., Ren, F., Chen, R., Meng, X., ... & Chen, W. (2022). Recent advances in the combined elevated temperature, humidity, and light stability of perovskite solar cells. Solar RRL, 6(12), 2200772.

Zhou, Y., Najar, A., Zhang, J., Feng, J., Cao, Y., Li, Z., ... & Liu, S. F. (2022). Effect of solvent residue in the thin-film fabrication on perovskite solar cell performance. ACS applied materials & interfaces, 14(25), 28729-28737.

Zhu, L., Zhang, J., Guo, Y., Yang, C., Yi, Y., & Wei, Z. (2021). Small exciton binding energies enabling direct charge photogeneration towards low-driving-force organic solar cells. Angewandte Chemie, 133(28), 15476-15481.

Zhu, W., Wang, S., Zhang, X., Wang, A., Wu, C., & Hao, F. (2022). Ion migration in organic–inorganic hybrid perovskite solar cells: current understanding and perspectives. Small, 18(15), 2105783.

Znidi, F., Morsy, M., & Uddin, M. N. (2024). Navigating challenges and solutions for metal-halide and carbon-based electrodes in perovskite solar cells (NCS-MCEPSC): An environmental approach. Heliyon, 10(12).

Zou, Q., Lin, Z., Li, Z., Hu, G., Zhou, S., Zheng, Y., ... & Yang, J. (2025). Closed-loop recycling of lead iodide precursor from waste organic solvents in the production of perovskite solar cells: Toward sustainable photovoltaics. Waste Management, 206, 115049.

APPENDICES

Appendix I: Python source code for IV characteristics

```
import matplotlib.pyplot as plt
#import pandas as pd
#import pygal

# Generating some sample data
voltage = []
current = []
power = []
f = open("pviv_co1.txt", encoding='cp1252')
for line in f:
        lines = [i for i in line.split()]
        current.append(float(lines[3])*-1)
        power.append(float(lines[5])*-1)
        voltage.append(float(lines[0]))

# Creating the plot
fig, ax1 = plt.subplots()

color = 'tab:red'
ax1.set_xlabel('Voltage(V)', fontsize = 14)
ax1.set_ylabel('Power(mW)', color=color, fontsize = 14)
ax1.plot(voltage, power, color=color)
ax1.set_yscale('log')
ax1.tick_params(axis='y', labelcolor=color)

ax2 = ax1.twinx()
color = 'tab:blue'
ax2.set_ylabel('Current (mA)', color=color , fontsize = 14)
```

```
ax2.plot(voltage, current, color=color)
ax2.set_yscale('log')
ax2.tick_params(axis='y', labelcolor=color)
plt.xlim()
plt.legend()
plt.xscale('log')

#plt.title('Power and Current vs Voltage')
plt.savefig('pviv_co1_log.png', dpi = 1600)
fig.tight_layout()
plt.show()
```

Appendix II: Python source code for RAT spectra

```
import matplotlib.pyplot as plt
#import numpy as np
Wavelength = []
Transmittance_T = []
Reflectance_R = []
Absorbance_A = []
f = open("testsample5.txt", encoding='cp1252')
for line in f:
    lines = [float(i) for i in line.split()]
    Wavelength.append(lines[0])
    Transmittance_T.append(lines[1])
    Reflectance_R.append(lines[11])
    Absorbance_A.append(lines[3])
fig, ax1 = plt.subplots()
color1 = 'tab:red'
color2 = 'tab:blue'
color3 = 'tab:green'
ax1.set_xlabel('$\lambda$(nm)', fontsize=16)
```

```
# Plot Reflectance
ax1.set_ylabel('R(%)', color=color1, fontsize=16)
ax1.plot(Wavelength, Reflectance_R, label='%R', color=color1)
ax1.tick_params (axis='y', labelcolor=color1)
# Plot Transmittance
ax2 = ax1.twinx()
ax2.set_ylabel('T(%)', color=color2, fontsize=16)
ax2.plot(Wavelength, Transmittance_T, label='%T', color=color2)
ax2.tick_params (axis='y', labelcolor=color2)
# Plot Absorbance
ax3 = ax1.twinx()
ax3.spines['right'].set_position(('outward', 60))  # Move the third axis to the right
ax3.set_ylabel('A(a.u.)', color=color3, fontsize=16)
ax3.plot(Wavelength, Absorbance_A, label='A', color=color3)
ax3.tick_params(axis='y', labelcolor=color3)
# Adjust the y-axis scales for better visibility
ax1.set_ylim(0, max(Reflectance_R) + 5)
ax2.set_ylim(0, max(Transmittance_T) + 5)
ax3.set_ylim(0, max(Absorbance_A) + 0.1)
#plt.title('Wavelength vs %T, %R, & A', fontsize=16)
fig.tight_layout()
plt.savefig('TRA.png', dpi=1600)
plt.show()
```

Appendix III: Python Script for SEM image segmentation

```
# -*- coding: utf-8 -*-
"""
@author: Silas
"""

import cv2
```

```
import numpy as np
import matplotlib.pyplot as plt
from skimage import measure, morphology
from skimage.segmentation import watershed
import pandas as pd
from scipy.stats import linregress

plt.style.use("seaborn-v0_8")

def calculate_grain_sizes(image_path, pixels_per_nm, min_grain_size=50):
    """Calculate grain sizes in nanometers"""
    img = cv2.imread(image_path, cv2.IMREAD_GRAYSCALE)
    if img is None:
        raise ValueError("Image not found or invalid path!")

    blurred = cv2.bilateralFilter(img, 9, 75, 75)
    clahe = cv2.createCLAHE(clipLimit=4.0, tileGridSize=(8,8))
    enhanced = clahe.apply(blurred)

    binary = cv2.adaptiveThreshold(enhanced, 255,
                                   cv2.ADAPTIVE_THRESH_GAUSSIAN_C,
                                   cv2.THRESH_BINARY_INV, 11, 2)

    kernel = morphology.disk(2)
    opened = cv2.morphologyEx(binary, cv2.MORPH_OPEN, kernel, iterations=2)
    cleaned = morphology.remove_small_objects(opened.astype(bool),
                                              min_size=min_grain_size)

    distance = cv2.distanceTransform(cleaned.astype(np.uint8), cv2.DIST_L2, 5)
    markers = measure.label(cleaned)
    ws = watershed(-distance, markers, mask=cleaned)
```

```
    props = measure.regionprops(ws, intensity_image=img)

    results = []
    for grain in props:
        area_nm2 = grain.area / (pixels_per_nm**2)
        diameter_nm = 2 * np.sqrt(area_nm2 / np.pi)
        results.append({
            'Area_nm2': area_nm2,
            'Diameter_nm': diameter_nm,
            'Circularity': (4 * np.pi * grain.area) / (grain.perimeter**2 + 1e-6),
            'Solidity': grain.solidity,
            'Mean_Intensity': grain.mean_intensity
        })

    return pd.DataFrame(results), (img, ws)

def plot_results_nm(df, images, save=True):
    """Visualization with nm units and publication-ready figures"""
    fig, ax = plt.subplots(2, 2, figsize=(15, 12), dpi=600)

    # Labels for subplots
    labels = ["(a)", "(b)", "(c)", "(d)"]
    positions = [(0,0), (0,1), (1,0), (1,1)]

    # Add subplot labels with white background (TOP CENTER)
    for label, (i, j) in zip(labels, positions):
        ax[i,j].text(0.5, 0.98, label, transform=ax[i,j].transAxes,
                     fontsize=16, fontweight="bold", va="top", ha="center",
                     bbox=dict(facecolor="white", alpha=0.8, edgecolor="none", pad=2))
```

```
    # Original image
    ax[0,0].imshow(images[0], cmap='gray')
    ax[0,0].set_title("Original SEM Image", fontsize=14, fontweight="bold")
    ax[0,0].axis("off")

    # Segmented grains
    ax[0,1].imshow(images[1], cmap='nipy_spectral')
    ax[0,1].set_title(f"Segmented Grains ({len(df)} detected)", fontsize=14,
fontweight="bold")
    ax[0,1].axis("off")

    # Grain size distribution
    bins = 30
    counts, edges, patches = ax[1,0].hist(df['Diameter_nm'], bins=bins, color='blue',
alpha=0.7)
    bin_width = edges[1] - edges[0]
    mean_val = df['Diameter_nm'].mean()
    std_val = df['Diameter_nm'].std()

    ax[1,0].set_xlabel("Grain Diameter (nm)", fontsize=14, fontweight="bold")
    ax[1,0].set_ylabel("Frequency (Count)", fontsize=14, fontweight="bold")
    ax[1,0].set_title(
        f"Size Distribution\nMean: {mean_val:.0f} ± {std_val:.0f} nm\nBin width:
{bin_width:.1f} nm",
        fontsize=13, fontweight="bold"
    )
    ax[1,0].tick_params(axis='both', labelsize=14, width=2, length=6)
    for label in ax[1,0].get_xticklabels() + ax[1,0].get_yticklabels():
        label.set_fontweight("bold")

    # Circularity vs Diameter
```

```
    x = df['Diameter_nm']
    y = df['Circularity']
    sc = ax[1,1].scatter(x, y, c=df['Solidity'], cmap='viridis', alpha=0.7, label="Grains")

    slope, intercept, r_value, _, _ = linregress(x, y)
    ax[1,1].plot(x, slope*x + intercept, color="red", lw=2,
                 label=f"Trendline (R²={r_value**2:.2f})")

    ax[1,1].set_xlabel("Diameter (nm)", fontsize=14, fontweight="bold")
    ax[1,1].set_ylabel("Circularity (1 = perfect circle)", fontsize=12, fontweight="bold")
    ax[1,1].set_title("Shape Characteristics", fontsize=14, fontweight="bold")
    ax[1,1].tick_params(axis='both', labelsize=14, width=2, length=6)
    for label in ax[1,1].get_xticklabels() + ax[1,1].get_yticklabels():
        label.set_fontweight("bold")

    ax[1,1].legend()
    cbar = plt.colorbar(sc, ax=ax[1,1])
    cbar.set_label("Solidity", fontsize=14, fontweight="bold")
    cbar.ax.tick_params(labelsize=14, width=2, length=6)
    for label in cbar.ax.get_yticklabels():
        label.set_fontweight("bold")

    plt.tight_layout()
    if save:
        plt.savefig('grain_analysis_results_cross10kx.png', dpi=800)
    plt.show()

if __name__ == "__main__":
    IMAGE_PATH = "pure PbJ2+MAI cross 10kx.tif"
    PIXELS_PER_NM = 0.05  # Example calibration
```

```
    print("Processing image...")
    df, images = calculate_grain_sizes(IMAGE_PATH, PIXELS_PER_NM)

    print("\n=== GRAIN ANALYSIS RESULTS (nm) ===")
    print(f"Total grains detected: {len(df)}")
    print(f"Average diameter: {df['Diameter_nm'].mean():.0f} ±
{df['Diameter_nm'].std():.0f} nm")
    print(f"Diameter range: {df['Diameter_nm'].min():.0f}-{df['Diameter_nm'].max():.0f}
nm")
    print(f"Average circularity: {df['Circularity'].mean():.3f} (1 = perfect circle)")

    df.to_csv("grain_size_analysis_cross10kx.csv", index=False)
    print("\nResults saved to:")
    print("- grain_size_analysis_cross10kx.csv")
    print("- grain_analysis_results_cross10kx.png")
      plot_results_nm(df, images)
```

Appendix IV: Python source code for Diffraction patterns

```
import numpy as np
import matplotlib.pyplot as plt
from scipy.signal import find_peaks
from matplotlib.ticker import FuncFormatter
# --- Data Loading ---
material = 'CH$_3$NH$_3$PbI$_3$'
theta, intensity = [], []
with open("MAPICB1.txt", encoding='cp1252') as f:
    for line in f:
        parts = line.split()
        theta.append(float(parts[0]))
        intensity.append(float(parts[2]))
# --- Peak Finding ---
```

```
peaks, _ = find_peaks(intensity, height=17000)
peak_labels = {
    14.1: '(110)', 28.3: '(220)',
    31.8: '(310)', 43.2: '(314)'
}
# --- Custom Formatter for "1×10³" Style ---
def sci_formatter(x, pos):
    """Format numbers as 'a×10ᵇ' with superscript exponents."""
    if x == 0:
        return '0'
    exponent = int(np.floor(np.log10(abs(x))))
    coeff = x / 10**exponent
    # Convert exponent to superscript (e.g., 3 → '³')
    superscript_map = {'0':'⁰', '1':'¹', '2':'²', '3':'³', '4':'⁴',
                       '5':'⁵', '6':'⁶', '7':'⁷', '8':'⁸', '9':'⁹'}
    exp_str = ''.join([superscript_map[d] for d in str(exponent)])
    return f"{coeff:.1f}×10{exp_str}"  # Added × symbol
# --- Plot Setup ---
plt.figure(figsize=(10, 6))
plt.plot(theta, intensity, 'k-', linewidth=1.5)
# --- Peak Annotations ---
for angle, label in peak_labels.items():
    peak_idx = min(peaks, key=lambda p: abs(theta[p] - angle))
    plt.annotate(label, (theta[peak_idx], intensity[peak_idx]),
                 xytext=(0, 10), textcoords="offset points",
                 ha='center', va='bottom', rotation=90,
                 fontsize=10, color='black')
# --- Axis Formatting ---
plt.gca().yaxis.set_major_formatter(FuncFormatter(sci_formatter))
plt.xlabel('2θ (°)', fontsize=16)
plt.ylabel('Intensity (Arb. un)', fontsize=16)
```

```
plt.ylim(0, 3.5e5)
plt.xlim(10, 50)
plt.tick_params(axis='both', which='major', labelsize=14)
plt.grid(True, linestyle=':', alpha=0.5)
plt.tight_layout()
#plt.savefig('MAPI_XRD.png', dpi=2000, bbox_inches='tight')
plt.show()
```

Appendix V: Glovebox Equipment



Appendix VI: The sonicator, spin coater and heater equipment



Appendix VII: Film Deposition in the MMUST Perovskite Laboratory

